Ensemble learning of foundation models for precision oncology

Xiangde Luo[1‡], Xiyue Wang[1‡], Feyisope Eweje[1], Xiaoming Zhang[2], Sen Yang[1], Ryan Quinton[3], Jinxi Xiang[1], Yuchen Li[1], Yuanfeng Ji[1], Zhe Li[1], Yijiang Chen[1], Colin Bergstrom[3], Ted Kim[1], Francesca Maria Olguin[3], Kelley Yuan[2], Matthew Abikenari[4], Andrew Heider[1], Sierra Willens[3], Sanjeeth Rajaram[3], Robert West[2], Joel Neal[3], Maximilian Diehn[1], Ruijiang Li[*1,5]

[1] *Department of Radiation Oncology, Stanford University School of Medicine, Stanford, CA, USA.*

[2] *Department of Pathology, Stanford University School of Medicine, Stanford, CA, USA*

[3] *Department of Medicine (Oncology), Stanford University School of Medicine, Stanford, CA, USA*

[4] *Department of Neurosurgery, Stanford University School of Medicine, Stanford, CA, USA*

[5] *Stanford Institute for Human-Centered Artificial Intelligence, Stanford, CA, USA*

‡ *equal contribution*

* *Correspondence to Ruijiang Li (**rli2@stanford.edu**).*

arXiv:2508.16085v1 [cs.CV] 22 Aug 2025

Funding This study was supported in part by the National Institutes of Health under research grants R01CA269559, R01CA285456 and R01CA290715 from the National Cancer Institute.

Abstract

Histopathology is essential for disease diagnosis and treatment decision-making. Recent advances in artificial intelligence (AI) have enabled the development of pathology foundation models that learn rich visual representations from large-scale whole-slide images (WSIs). However, existing models are often trained on disparate datasets using varying strategies, leading to inconsistent performance and limited generalizability. Here, we introduce ELF (**E**nsemble **L**earning of **F**oundation models), a novel framework that integrates five state-of-the-art pathology foundation models to generate unified slide-level representations. Trained on 53,699 WSIs spanning 20 anatomical sites, ELF leverages ensemble learning to capture complementary information from diverse models while maintaining high data efficiency. Unlike traditional tile-level models, ELF's slide-level architecture is particularly advantageous in clinical contexts where data are limited, such as therapeutic response prediction. We evaluated ELF across a wide range of clinical applications, including disease classification, biomarker detection, and response prediction to major anticancer therapies—cytotoxic chemotherapy, targeted therapy, and immunotherapy—across multiple cancer types. ELF consistently outperformed all constituent foundation models and existing slide-level models, demonstrating superior accuracy and robustness. Our results highlight the power of ensemble learning for pathology foundation models and suggest ELF as a scalable and generalizable solution for advancing AI-assisted precision oncology.

Source codes: `https://github.com/lilab-stanford/ELF`

Introduction

Histopathology is a cornerstone of clinical practice, offering critical insights into cellular morphology and tissue architecture. As the gold standard for disease diagnosis, it also plays a vital role in guiding prognosis and informing treatment decisions. With the growing availability of digitized whole-slide histopathology images and advances in computational power, artificial intelligence (AI) has emerged as a powerful tool for histopathology image analysis, which has significant implications for precision oncology[1–4]. Among the most promising developments in this field are pathology foundation models—large-scale models pretrained using self-supervised learning on vast collections of histopathology slides [5–11]. These models can be fine-tuned for a wide range of downstream clinical tasks, with the potential to enhance diagnostic accuracy, identify novel prognostic and predictive biomarkers, and support personalized treatment strategies[12–14].

There has been a rapid proliferation of pathology foundation models in the last few years, with at least 15 developed and counting[15]. These foundation models are typically trained on proprietary datasets with different training strategies[16,17], leading to model-specific biases and divergent performance across applications[18,19]. Indeed, recent benchmark studies[18,20,21] based on extensive evaluation have shown that the relative performance of pathology foundation models is highly variable across different tasks and even across datasets for the same task. In other words, no single foundation model outperformed others for all tasks. This creates a conundrum in the community about which foundation model one should use for a particular application.

There is an emerging interest in combining the relative strengths of different foundation models. One recent study attempted to resolve the differences among several existing models using knowledge distillation[19]. As a result, the model effectively learns an 'average' feature representation, which may paradoxically reduce feature diversity and representation capability of the resulting model. This approach did not outperform existing foundation models as shown in benchmark studies[20]. The optimal strategy that truly leverages the complementary value of different foundation models remains to be explored.

Here, we present ELF (Ensemble Learning of Foundation models), a new paradigm for integrating multiple foundation models. ELF incorporates five state-of-the-art pathology foundation models and generates a unified representation for the whole-slide image (WSI) through additional pretraining on 53,699 WSIs across 20 anatomical sites. As a pretrained slide-level foundation model, ELF has significant advantages over traditional tile-level foundation models in that it is much more data-efficient, and therefore, is particularly well suited to clinical applications where a sufficiently large dataset is not available for model fine-tuning. This is quite common in therapeutic response prediction which is focused on a particular drug regimen in a given indication and clinical setting.

We evaluated the performance of ELF on a wide range of clinical applications, including challenging disease diagnosis, molecular biomarker detection, and treatment response prediction. In particular, we tested ELF for predicting response across all major anticancer therapies including cytotoxic chemotherapy, molecularly targeted therapy, and immunotherapy in various cancer types. ELF achieved superior performance compared with each of the five individual foundation models as well as existing slide-level foundation models[5,6,22]. These findings demonstrate the effectiveness of our ensemble learning approach for integrating pathology foundation models, with broad implications in precision medicine.

Results

Design and evaluation of ensemble learning of foundation models

We proposed an ensemble learning approach (ELF) to integrate multiple independently trained foundation models into a single model (**Figure 1**). ELF generates a unified slide-level representation that combines the complementary strengths of five tile-level pathology foundation models: GigaPath[5], CONCH[10], Virchow2[23], H-Optimus-0[8], and UNI[9]. These five models were chosen because of the large number of slides used for pretraining (>100,000) and their generally top-ranking performance (though not always) across benchmark studies[18,20,21].

ELF was pretrained on 53,699 whole-slide images (WSIs) using unsupervised contrastive learning for feature alignment and weakly supervised learning for cancer detection and organ classification (**Figure 1a-b**). The architecture of ELF comprises two main components: (1) five pretrained tile-level feature extractors and (2) an ensemble module that synthesizes a unified slide representation. For inference, ELF processes a given slide through each base model to obtain per-model embeddings, which are then fused into a unified slide-level feature representation (**Figure 1c**). ELF was evaluated on a wide range of clinical applications, including classification and subtyping of 4,697 tumor samples, 88 combinations of biomarker-indication assessment in 11,530 patients, and therapeutic response prediction in 21 independent cohorts of 1,592 patients across 9 cancer types (**Figure 1c-d**). Detailed model architectures, training regimes, and evaluation protocols are provided in the Methods.

Disease classification and subtyping

We first evaluated ELF on challenging diagnostic problems for disease classification and subtyping. These included skin cancer subtyping (2 cls, 3 cls, and 5 cls, cls means classes) using the Basal Cell Carcinoma Classification (BCCC) dataset[24] (1,832 samples), breast cancer subtyping (7 cls) using the BReAst Carcinoma Subtyping (BRACS) dataset (547 samples)[25], and brain tumour subtyping (12 cls and 30 cls) using the EBRAINS dataset (2,319 samples)[26]. We compared ELF with three state-of-the-art slide-level foundation models (Prov-GigaPath[5], CHIEF[6], and TITAN[22]), using balanced accuracy (BA) as the evaluation metric.

ELF consistently achieved the highest performance across all tasks, surpassing the second-best model, TITAN, by an average of 2.2% across all datasets and up to 16.3% on BRACS (**Figure 2a**). Specifically, on the BCCC dataset, ELF achieved BA of 0.961 (95% confidence interval (CI): 0.941-0.979), 0.871 (95% CI: 0.8393-0.903), and 0.709 (95% CI: 0.663-0.752) on the 2-, 3-, and 5 cls subtyping tasks, respectively. These results exceeded all baseline models including TITAN (BA: 0.951, 0.868, and 0.700; $P < 0.001$ for all). Similarly, for brain tumour subtyping on EBRAINS, ELF achieved 0.907 (95% CI: 0.869-0.944) BA

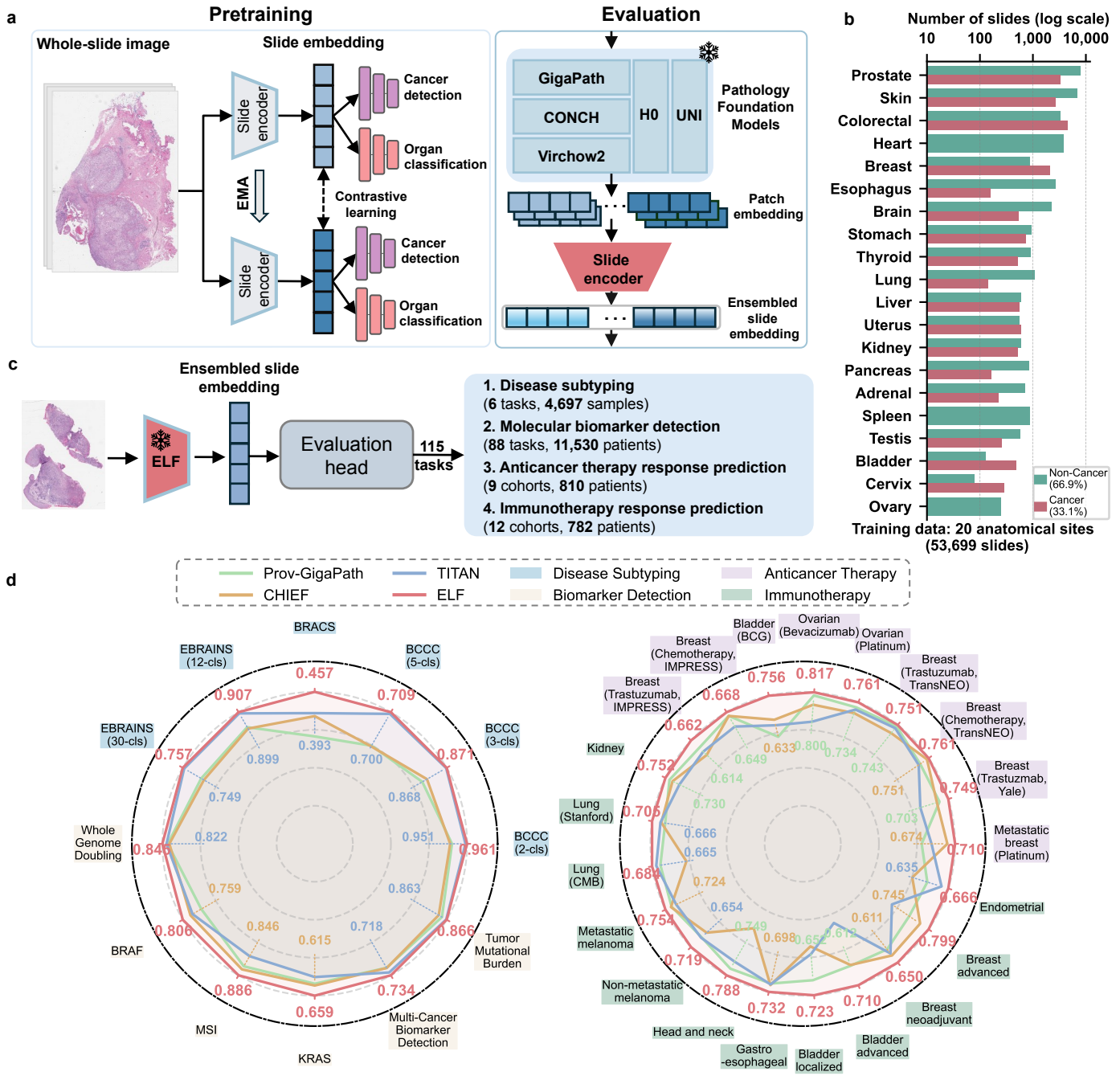


Figure 1: **ELF model design and evaluation. a,** Model pretraining. ELF is a new paradigm for integrating multiple foundation models through a unified slide-level pathology foundation model. Here, five independently trained tile-level foundation models were employed to construct this ensemble (GigaPath[5], CONCHV1.5[10], Virchow2[23], H-Optimus-0[8], UNI[9]). During pretraining, ELF employs contrastive learning to align slide embeddings derived from different foundation models applied to the same WSI, thereby capturing their complementary strengths. To further enhance pan-cancer representation learning, two auxiliary supervision tasks (cancer detection and organ classification) are incorporated in a multitask setting. An ensemble module integrates its outputs into a cohesive slide representation. **b,** Data distribution for ELF pretraining, which consists of 53,699 slides with clinical information across 20 anatomical sites from 11 public datasets. **c,** ELF is evaluated across diverse clinical applications, including disease subtyping, biomarker detection, and response prediction for anticancer therapy and immunotherapy. **d,** Across these clinical tasks, ELF consistently outperforms three leading slide-level pathology foundation models (Prov-GigaPath[5], CHIEF[6], and TITAN[22]). Performance is reported using balanced accuracy (BA) for disease subtyping, and area under the ROC curve (AUC) for biomarker detection and treatment response prediction.

(12 cls) and 0.757 (95% CI: 0.716-0.795) (30 cls), outperforming TITAN by around 1% ($P < 0.001$). The improvements in classification performance were more notable for challenging tasks. On the BRACS dataset (7 cls breast subtyping), ELF achieved a BA of 0.457 (95% CI: 0.359-0.566), representing a 16.3% relative improvement over TITAN (0.393), and substantially outperforming other models such as CHIEF (0.384) and Prov-GigaPath (0.323) ($P < 0.001$).

To assess the quality of slide-level representations, we performed t-SNE visualization of slide embeddings generated by ELF and Prov-GigaPath, which are both pure vision encoders. Using the EBRAINS dataset (12 cls) as an example, we evaluated their ability to separate histological subtypes in the embedding space (**Figure 2b**). ELF produced more distinct and coherent clusters corresponding to known brain tumor subtypes, including ependymal, lymphoid, and sellar tumors . These patterns were consistently observed in both development (the combined training and validation sets) and test sets. More detailed comparisons were presented in **Extended Data Figure 1a, b**. Such well-separated histological representations contribute to improved classification accuracy of known disease subtypes and might facilitate unsupervised discovery of new disease categories.

To understand the reason behind ELF's superior performance, we conducted an ablation study to examine two key design factors: the integration of diverse foundation models and the ensemble strategy. First, we evaluated whether combining different foundation models yields better performance than using any single model alone. On the BRACS dataset (7 cls), ELF achieved a BA of 0.457, substantially higher than any individual foundation models, including GigaPath with a BA of 0.323; $P < 0.001$; **Figure 2c**. Similarly, on EBRAINS (30 cls), ELF achieved a BA of 0.757, outperformed the best individual model, Virchow2, with a BA of 0.702 ($P < 0.001$; **Figure 2c**). Interestingly, no single model outperformed any other individual models in these two tasks. Second, we evaluated the effectiveness of our ensemble approach against standard tile aggregation strategies, including mean pooling and max pooling. On BRACS, ELF (BA: 0.457) outperformed mean pooling (BA: 0.328) and max pooling (BA: 0.317) by a large margin ($P < 0.001$; **Figure 2d**). Similarly, on EBRAINS (30 cls), ELF (0.757) again outperformed both mean pooling (BA: 0.705) and max pooling (BA: 0.703; $P < 0.001$; **Figure 2d**).

ELF integrates diverse pathology foundation models by leveraging their complementary representations of morphological features. A potential hypothesis is that each model may focus on distinct histological regions. To test this, we extracted tile-level embeddings from each individual foundation model and passed them through ELF's slide encoder to obtain attention scores for each tile. We then computed pairwise Pearson correlations between the attention maps generated by different models. The results revealed consistently low correlations, suggesting that different models indeed focus on non-overlapping morphological regions (**Extended Data Figure 2a**). Besides, we further extracted slide-level embeddings based on each individual foundation

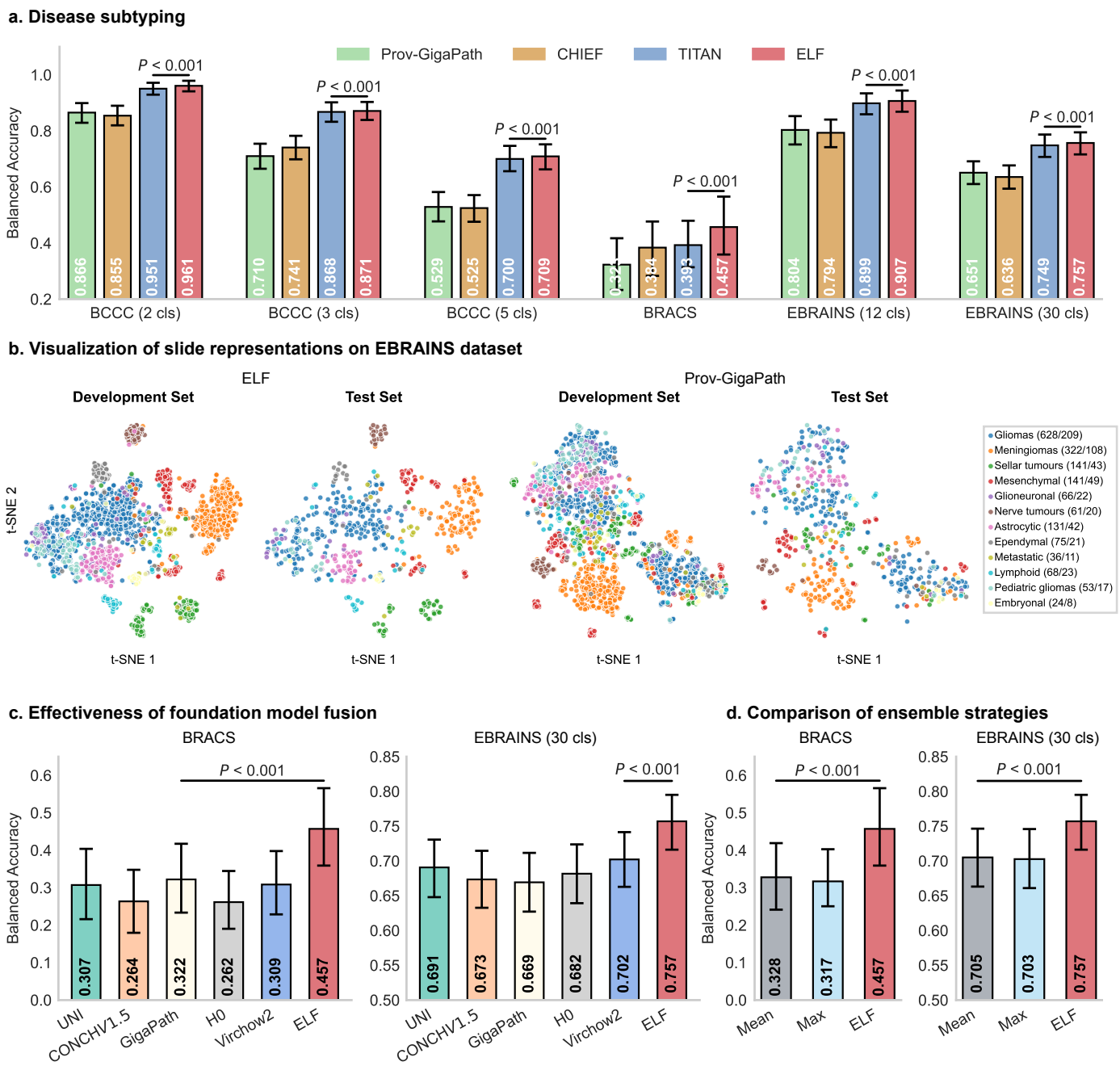


Figure 2: **Disease classification and subtyping. a,** Performance evaluation on six disease subtyping tasks. ELF consistently outperforms three state-of-the-art foundation models (Prov-GigaPath, CHIEF, TITAN) across three datasets (BCCC, BRACS, and EBRAINS), with statistically significant gains in balanced accuracy (all $P < 0.001$). **b,** Visualization of slide-level feature representations. t-SNE maps show that ELF generates more separable and coherent disease clusters than Prov-GigaPath on the EBRAINS dataset (12 cls), revealing improved subtype-specific structure in both development and test sets. **c,** ELF significantly outperformed individual foundation models for disease subtyping ($P < 0.001$), confirming the effectiveness of foundation model fusion. **d,** The ELF ensemble learning strategy significantly outperformed alternative aggregation methods using the same five tile-level foundation models ($P < 0.001$). Statistical significance was assessed using a two-sided Wilcoxon signed-rank test. All results are presented as means with 95% CIs obtained from 1,000 bootstrap replicates.

model's tile-level embedding through ELF's slide encoder and measured their correlation (**Extended Data Figure 2b**). The results indicated extremely low correlations, highlighting that different models encode the patch in variant ways. These findings highlight ELF's ability to integrate diverse histological perspectives, supporting its superior accuracy in complex disease classification and subtyping tasks.

Molecular biomarker detection

Recent advances in computational pathology have demonstrated the feasibility of predicting therapeutically relevant biomarkers directly from routine H&E-stained slides, which may accelerate treatment decisions[28]. To systematically evaluate ELF's capability in this context, we conducted a large-scale study using the TCGA pan-cancer cohort, which includes 28 clinically actionable genetic alterations spanning 13 cancer types and approximately 6,500 patients[29]. On the TCGA benchmark, ELF achieved a mean area under the receiver operating characteristic curve (AUC) of 0.734 $\pm$ 0.091 across 74 biomarker-indication combinations, significantly surpassing prior foundation models, including TITAN (0.718 $\pm$ 0.099), CHIEF (0.693 $\pm$ 0.101), and Prov-GigaPath (0.692 $\pm$ 0.106) (P = 0.034, two-sided Wilcoxon test comparing TITAN versus ELF; **Figure 3a**). A heatmap visualization further illustrates ELF's biomarker prediction performance for individual tasks, with a high accuracy (AUC $>$ 0.85) for clinically actionable biomarkers, such as *BRAF* mutation in thyroid and colorectal cancers, *KRAS* and *ROS1* mutations in lung cancer, *IDH1* and *FGFR3* mutations in gliomas (**Figure 3b**).

Identifying MSI as well as *BRAF*/*KRAS* mutation status represents a fundamental part of the diagnostic workup and treatment of metastatic colorectal cancer (CRC). To further evaluate generalizability across diverse patient populations in this clinically relevant domain, we conducted external validation of ELF for predicting *BRAF*, *KRAS* mutations, and MSI status using four CRC cohorts: SR386[30], SR1482[30], MCO[31,32], and TCGA-CRC[29], comprising a total of 2,711 patients. Among them, SR386, a recently released real-world dataset, was used for internal cross-validation, while SR1482, MCO, and TCGA-CRC served as external validation cohorts. For *BRAF* mutation prediction, ELF consistently outperformed competing models across four cohorts with an average AUC of 0.806 ± 0.021. Specifically, the performance on three external cohorts was 0.777 ± 0.033 (SR1482), 0.842 ± 0.014 (MCO), and 0.763 ± 0.031 (TCGA-CRC), respectively. These represented notable AUC improvements ranging up to 13% compared to the existing model CHIEF[6] (P < 0.01; **Figure 3c**, top row, and detailed comparison results were presented **Extended Data Figure 4a**). For MSI status prediction, ELF achieved excellent performance with an average AUC of 0.886 ± 0.015 across the four cohorts. Specifically, the results on three external cohorts were 0.869 ± 0.042 (SR1482), 0.897 ± 0.013 (MCO), 0.855 ± 0.028 (TCGA-CRC), respectively, consistently exceeding the second-best model (CHIEF) up to 7% (P < 0.01; **Figure 3c**, bottom row, **Extended Data Figure 4b**). Similar patterns were observed for *KRAS* mutation prediction (**Extended Data Figure 4c**). To assess the clinical utility of these results, we computed the positive predictive

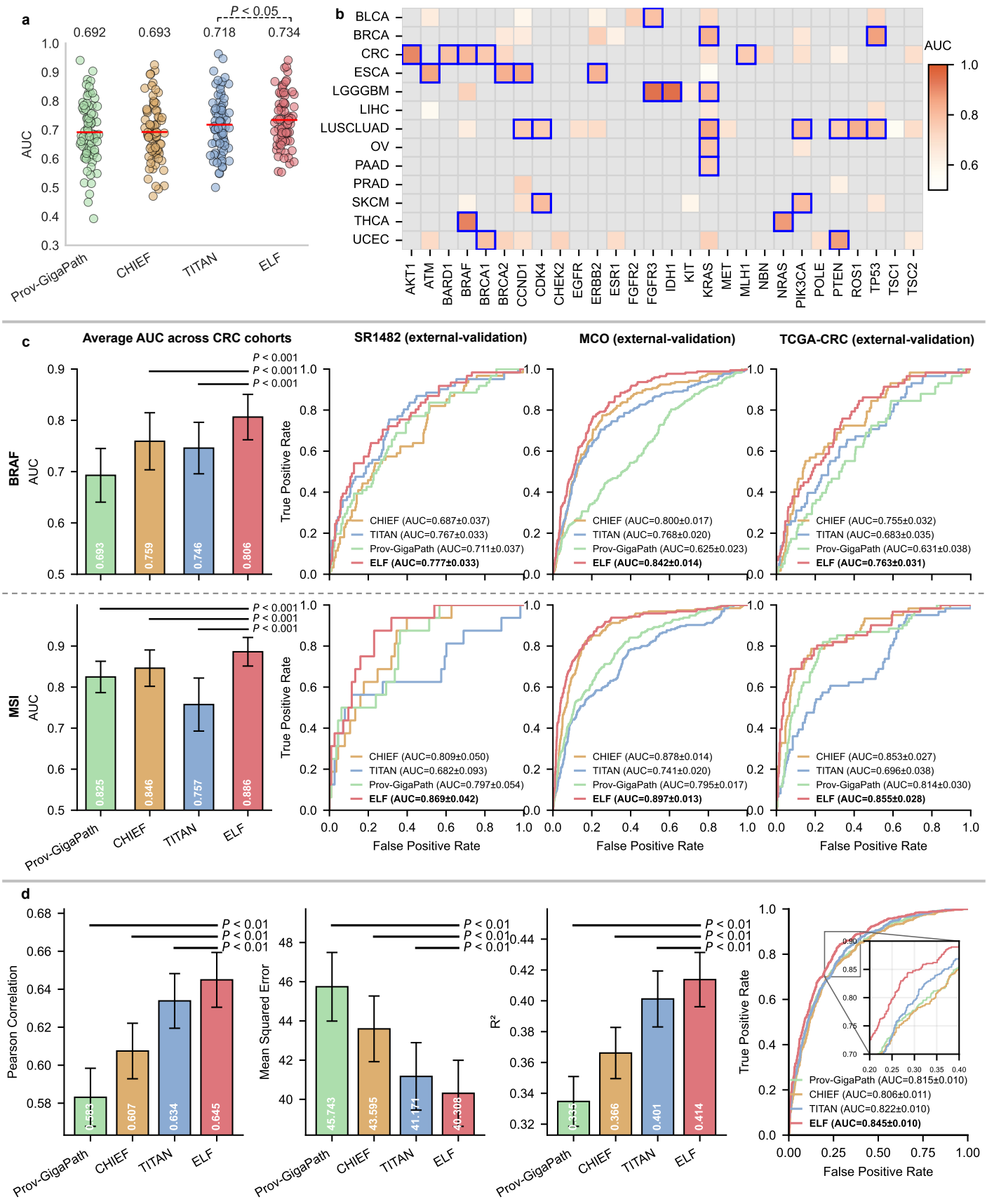

a
P < 0.05
0.692
0.693
0.718
0.734
AUC
Prov-GigaPath
CHIEF
TITAN
ELF
b
BLCA
BRCA
CRC
ESCA
LGGGBM
LIHC
LUSCLUAD
OV
PAAD
PRAD
SKCM
THCA
UCEC
AUC
AKT1
ATM
BARD1
BRAF
BRCA1
BRCA2
CCND1
CDK4
CHEK2
EGFR
ERBB2
ESR1
FGFR2
FGFR3
IDH1
KIT
KRAS
MET
MLH1
NBN
NRAS
PIK3CA
POLE
PTEN
ROS1
TP53
TSC1
TSC2
c
Average AUC across CRC cohorts
SR1482 (external-validation)
MCO (external-validation)
TCGA-CRC (external-validation)
BRAF AUC
MSI AUC
P < 0.001
True Positive Rate
False Positive Rate
CHIEF (AUC=0.687±0.037)
TITAN (AUC=0.767±0.033)
Prov-GigaPath (AUC=0.711±0.037)
ELF (AUC=0.777±0.033)
CHIEF (AUC=0.800±0.017)
TITAN (AUC=0.768±0.020)
Prov-GigaPath (AUC=0.625±0.023)
ELF (AUC=0.842±0.014)
CHIEF (AUC=0.755±0.032)
TITAN (AUC=0.683±0.035)
Prov-GigaPath (AUC=0.631±0.038)
ELF (AUC=0.763±0.031)
CHIEF (AUC=0.809±0.050)
TITAN (AUC=0.682±0.093)
Prov-GigaPath (AUC=0.797±0.054)
ELF (AUC=0.869±0.042)
CHIEF (AUC=0.878±0.014)
TITAN (AUC=0.741±0.020)
Prov-GigaPath (AUC=0.795±0.017)
ELF (AUC=0.897±0.013)
CHIEF (AUC=0.853±0.027)
TITAN (AUC=0.696±0.038)
Prov-GigaPath (AUC=0.814±0.030)
ELF (AUC=0.855±0.028)
d
Pearson Correlation
Mean Squared Error
R²
P < 0.01
Prov-GigaPath (AUC=0.815±0.010)
CHIEF (AUC=0.806±0.011)
TITAN (AUC=0.822±0.010)
ELF (AUC=0.845±0.010)

Figure 3: **Therapeutic biomarker detection. a,** Overall performance comparison of biomarker detection across 74 74 biomarker-indication combinations in the TCGA dataset, including 13 cancer types and 28 biomarkers. ELF significantly outperformed Prov-GigaPath, CHIEF, and TITAN in AUC ($P < 0.05$). **b,** Heatmap showing ELF's AUC performance for individual biomarker prediction tasks in TCGA. Blue-outlined box highlighted biomarkers with AUC > 0.75 and at least 5 positive samples. **c,** ELF achieves superior performance for detecting *BRAF* mutation and MSI status across one internal and three external colorectal cancer (CRC) cohorts (SR386, SR1482, MCO, TCGA-CRC). Left bar plots show average performance across cohorts; ROC curves display external validation results. **d,** Performance comparison on the aneuploidy score regression (the left three panels) and whole-genome doubling classification (the right panel) tasks. ELF surpasses all baseline models across Pearson correlation, mean squared error (MSE), R^2, and AUC (based on whole-genome doubling positive *vs* negative[27]). Barplot in **c**-**d** were presented as mean value with standard error across five-fold validation or all cohorts. ROC curves and associated metrics in **c**-**d** were presented as the mean value with standard deviation estimated by the bootstrap method (1,000 replicates). All statistical comparisons were conducted using two-sided Wilcoxon signed-rank tests.

value at high negative predictive value (i.e., rule-out) for biomarker detection (**Extended Data Table 9**). In the largest MCO external validation dataset, ELF achieved PPV of 0.35 and 0.55 for *BRAF* mutation and MSI detection at NPV of 0.95, which is significantly higher than alternative models.

In addition to mutation status prediction, we further evaluated ELF on a continuous regression task for predicting aneuploidy scores. Aneuploidy, when cells harbor abnormal numbers of chromosomes, is a near-universal characteristic of tumor cells with significant clinical implications and for which reliable biomarkers are lacking. Aneuploidy is also inversely correlated with the expression of immune-related genes and a marker of immune evasion and resistance to immunotherapy[27]. We evaluated this task using the pan-cancer TCGA dataset, comprising 8,819 patients across 32 cancer types, with aneuploidy scores obtained from a prior study[27]. The results showed that ELF achieved better performance than three existing methods across three regression evaluation metrics (**Figure 3d** the first three panels). Specifically, ELF achieved the highest Pearson correlation (0.645 ± 0.014), the lowest mean squared error (40.308 ± 1.687), and the greatest coefficient of determination ($R^2 = 0.414 \pm 0.018$); all pairwise improvements were significant at $P < 0.01$.

Besides, we evaluated the performance of ELF for the detection of whole-genome doubling[27], an early oncogenic event with prognostic and therapeutic implications as well as driver of chromosomal instability[33,34] (**Figure 3d** the right panels). ELF achieved superior AUC of 0.845 ± 0.010 (all $P < 0.001$), compared with 0.822 ± 0.010 (TITAN), 0.806 ± 0.011 (CHIEF) and 0.815 ± 0.010 (Prov-GigaPath). The ablation study investigated the performance of integrations of diverse foundation models and the ensemble strategy on the largest pan-cancer regression/classification tasks, encouraging the effectiveness of the ensemble strategy (**Extended Data Figure 5**). Finally, we evaluated the performance of ELF for the prediction of tumor mutational burden (TMB), a clinically actionable biomarker with predictive and therapeutic implications as well as an FDA-recognized determinant of immunotherapy response[35,36] (**Extended Data Figure 6**). The results showed that

ELF can predict TMB status accurately with an AUC > 0.86. And, ELF achieved the best PPV of 0.266 at NPV > 0.95 than others, highlighting its potential clinical utility. These results demonstrate ELF's enhanced capability to capture chromosomal instability–related histomorphological patterns.

Anticancer therapy response prediction

Accurate prediction of therapy response is crucial for personalized treatment but remains an unmet need due to inherent complexity and challenges [37,38]. To address this, we investigated ELF's ability to predict patient response across multiple anticancer therapy settings, including both chemotherapy-based and targeted treatments, spanning four cancer types and nine cohorts with a total of 810 patients. These datasets represent diverse treatment regimens and contexts, including platinum-based chemotherapy, trastuzumab- and bevacizumab-based targeted therapy, and Bacillus Calmette–Guérin (BCG)-based therapy in neoadjuvant, adjuvant, and advanced settings.

For chemotherapy response prediction, ELF demonstrated strong performance in metastatic breast cancer (Metastatic breast (Platinum), N = 77)[39] and high-grade serous ovarian cancer Ovarian (Platinum), N = 158)[40], achieving AUCs of 0.710 ± 0.032 and 0.761 ± 0.018, respectively (**Figure 4a**). For targeted therapy, ELF achieved similarly high performance in Breast (Trastuzumab, Yale)[41] breast patients treated with trastuzumab (AUC = 0.749 ± 0.040, N = 85) and Ovarian (Bevacizumab)[42] patients treated with bevacizumab (AUC = 0.817 ± 0.076, N = 36). In the Bladder (BCG) cohort (N = 131)[43], ELF achieved an AUC of 0.756 ± 0.025 for predicting BCG response. Across all five cohorts, ELF achieved an overall mean AUC of 0.759, significantly outperforming existing slide-level foundation models by 10-19% (all $P < 0.001$) (**Figure 4a**).

To assess whether ELF predictions reflect clinically meaningful outcomes, we performed Kaplan–Meier survival analysis in three cohorts with recurrence-free survival (RFS) and progression-free survival (PFS) data. ELF risk scores successfully stratified patients into high-risk and low-risk groups, with significant hazard ratios: Bladder (BCG) (HR = 2.05; 95% CI, 1.14–3.69; $P = 0.014$), Metastatic breast (platinum) (HR = 1.64; 95% CI, 1.02–2.63; $P = 0.04$), and Ovarian (Bevacizumab) (HR = 3.70; 95% CI, 1.31–10.45; $P = 0.0095$), further supporting the clinical relevance of ELF predictions (**Figure 4b**).

To evaluate model generalizability, we conducted cross-institutional validation using two additional breast cancer studies (TransNEO[44] and IMPRESS[45]). In the external validation cohort (IMPRESS, N = 64), ELF achieved an AUC of 0.668 (95% CI: 0.515-0.806) for predicting pathologic complete response (pCR) to neoadjuvant chemotherapy, surpassing previous foundation model models by 3-13% (all $P < 0.001$; **Figure 4c**, right). In another breast cohort, ELF reached an AUC of 0.662 (0.530–0.790) for predicting pCR to neoadjuvant trastuzumab in the external validation cohort (IMPRESS, N = 62), again outperforming baseline models

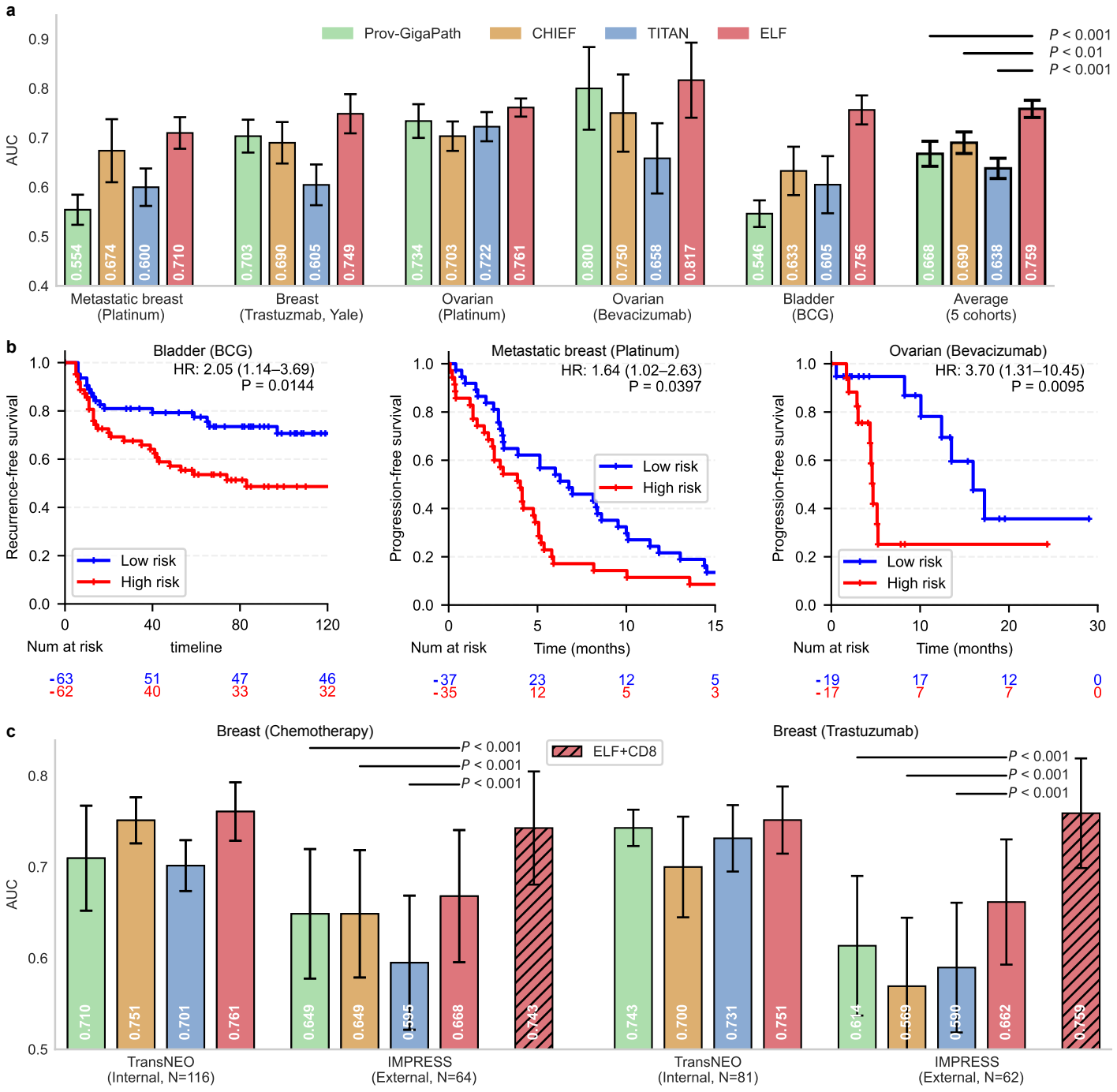


Figure 4: **Anticancer therapy response prediction. a,** Performance comparison of ELF and baseline models (Prov-GigaPath, CHIEF, TITAN) across five cohorts in predicting therapy response. These include chemotherapy (metastatic breast and ovarian with platinum), molecularly targeted therapy (breast with trastuzumab from Yale, Ovarian with Bevacizumab), and BCG response (bladder). ELF consistently achieves the highest AUC across all cohorts ($P < 0.001$). **b,** Kaplan–Meier analyses based on ELF-derived risk scores stratify recurrence-free survival in Bladder (BCG) and progression-free survival (PFS) in metastatic breast and ovarian cohorts. A two-sided log-rank test was used to compare survival outcomes between the high-risk and low-risk groups. **c,** Generalizability of ELF in neoadjuvant chemotherapy and trastuzumab response prediction using internal (TransNEO) and external (IMPRESS) cohorts. ELF maintains robust performance across all settings and significantly outperforms baseline models (all $P < 0.001$). A combination of ELF with CD8 further improved the accuracy for response prediction. In **a** and **c**, Bar plots were presented as mean value with standard error across five-fold validation or mean value with standard error estimated by the bootstrap method (1,000 replicates) for external validation cohorts. Statistical comparisons used two-sided Wilcoxon signed-rank tests.

by 8-16% (**Figure 4c**, left). Combining H&E-based ELF-predicted score with CD8[45] significantly improved the AUC to 0.743 and 0.759 for predicting response to neoadjuvant chemotherapy and trastuzumab, respectively. Besides, the ablation study investigated the performance of integrating diverse foundation models and the ensemble strategy on two external cohorts, also demonstrating the effectiveness of the ensemble strategy (**Extended Data Figure 7**).

Immunotherapy response prediction

Immunotherapy with immune checkpoint inhibitors (ICIs) has reshaped cancer treatment and is a standard of care in most tumor types. However, clinical response remains heterogeneous across patients, and reliable predictive biomarkers are lacking[46,47]. To address this, we evaluated ELF's ability to predict durable response to ICIs (defined as progression-free survival or PFS $\geq$ 6 months)[48,49] using pretreatment H&E-stained images in a real-world dataset consisting of 12 independent cohorts of 782 patients across eight cancer types. Among these, 11 cohorts were obtained from patients treated at Stanford Medicine, with 1 additional cohort from the Cancer Moonshot Project.

First, we analyzed eight internal cohorts of bladder cancer (localized, N = 47 and advanced, N = 46), endometrial cancer (advanced, N = 96), gastroesophageal adenocarcinoma (advanced, N = 106), head and neck cancer (advanced, N = 47), melanoma (non-metastatic, N = 63 and metastatic, N = 78), and renal cell carcinoma, a major subtype of kidney cancer (advanced, N = 52). Across these eight cohorts of six cancer types, ELF achieved a mean AUC of 0.731, and consistently demonstrated superior predictive performance over existing foundation models (Prov-GigaPath, CHIEF, TITAN) with mean AUCs ranging from 0.608 to 0.672 (all $P < 0.05$; **Figure 5a**).

To assess generalizability across patient cohorts, we further evaluated ELF on independent validation cohorts in breast cancer and non-small-cell lung cancer (NSCLC). In breast cancer, ELF achieved AUC = 0.650 ± 0.073 for predicting pCR after neoadjuvant immunotherapy and AUC = 0.799 ± 0.078 in an independent validation cohort of advanced breast cancer, significantly outperforming existing foundation models by up to 40% compared with TITAN ($P < 0.001$; **Figure 5c**, left). In NSCLC, ELF achieved AUC = 0.705 ± 0.027 on the Stanford cohort (N = 148) and 0.684 ± 0.098 on the external cohort (N = 34) from the Cancer Moonshot Project[50], again outperforming existing foundation models by up to 29% compared with CHIEF ($P < 0.001$; **Figure 5b**, left). In a subset of NSCLC patients (N=101) with PD-L1 expression data available, combining ELF scores with PD-L1 further improved predictive performance to AUC = 0.773 compared to ELF (0.732) and PD-L1 (0.679) alone. In the multivariable analysis, the ELF risk score remained the strongest independent predictor of durable response ($P < 0.01$; **Figure 5b**, right) adjusting for age, sex, smoking history, CNS metastasis, BMI, and PD-L1 status. Moreover, the ablation study investigated the performance of integrations of diverse

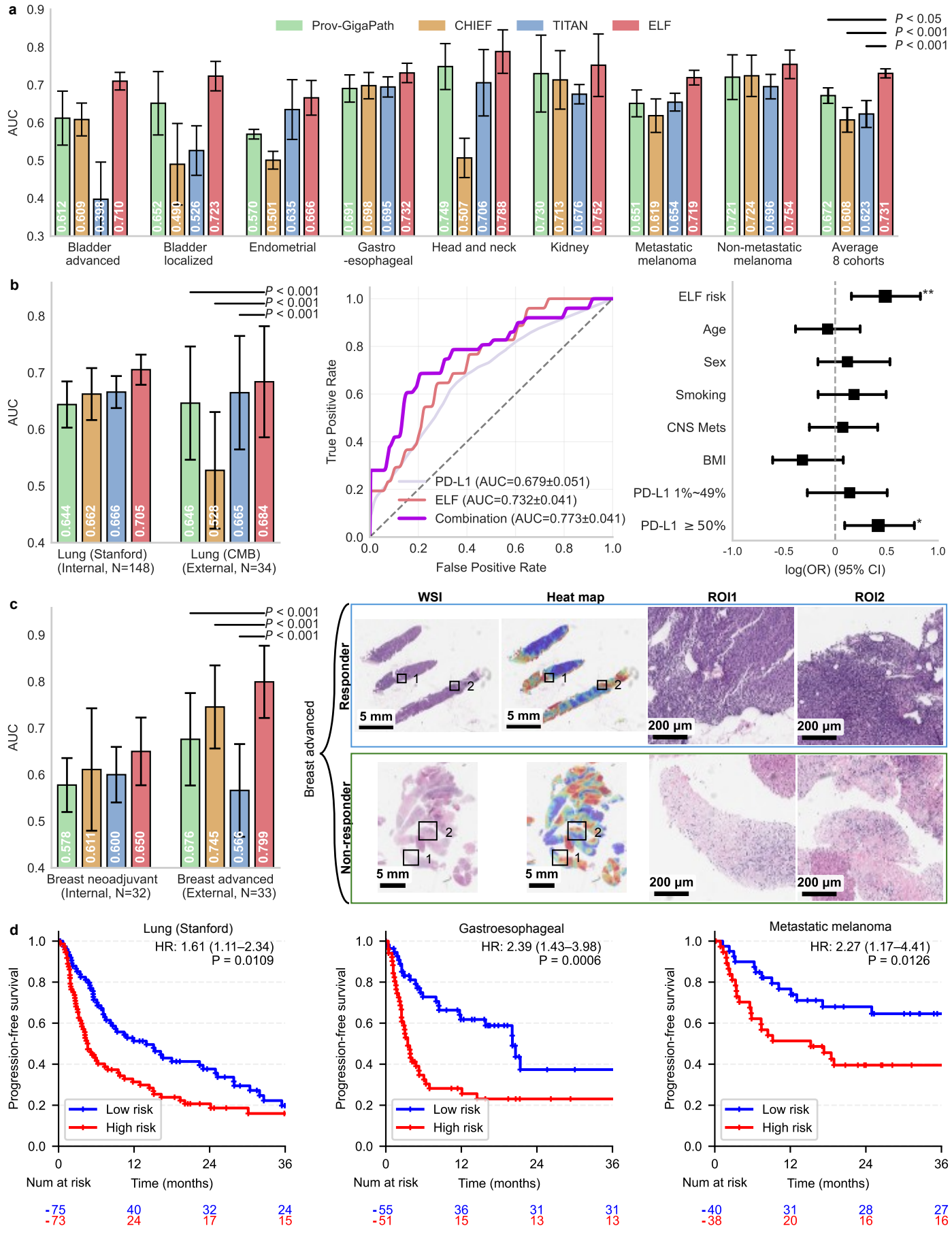

a
Prov-GigaPath
CHIEF
TITAN
ELF
P < 0.05
P < 0.001
P < 0.001
AUC
0.612 0.609 0.398 0.710
0.652 0.490 0.526 0.723
0.570 0.501 0.635 0.666
0.691 0.698 0.695 0.732
0.749 0.507 0.706 0.788
0.730 0.713 0.676 0.752
0.651 0.619 0.654 0.719
0.724 0.724 0.696 0.754
0.672 0.608 0.623 0.731
Bladder advanced
Bladder localized
Endometrial
Gastro -esophageal
Head and neck
Kidney
Metastatic melanoma
Non-metastatic melanoma
Average 8 cohorts
b
P < 0.001
P < 0.001
P < 0.001
AUC
0.644 0.662 0.666 0.705
0.646 0.526 0.665 0.684
Lung (Stanford) (Internal, N=148)
Lung (CMB) (External, N=34)
True Positive Rate
False Positive Rate
PD-L1 (AUC=0.679±0.051)
ELF (AUC=0.732±0.041)
Combination (AUC=0.773±0.041)
ELF risk
Age
Sex
Smoking
CNS Mets
BMI
PD-L1 1%~49%
PD-L1 ≥ 50%
log(OR) (95% CI)
c
P < 0.001
P < 0.001
P < 0.001
AUC
0.578 0.611 0.600 0.650
0.676 0.745 0.566 0.799
Breast neoadjuvant (Internal, N=32)
Breast advanced (External, N=33)
WSI
Heat map
ROI1
ROI2
Responder
Non-responder
Breast advanced
5 mm
200 μm
d
Lung (Stanford)
HR: 1.61 (1.11–2.34)
P = 0.0109
Gastroesophageal
HR: 2.39 (1.43–3.98)
P = 0.0006
Metastatic melanoma
HR: 2.27 (1.17–4.41)
P = 0.0126
Progression-free survival
Low risk
High risk
Num at risk
Time (months)
-75 40 32 24
-73 24 17 15
-55 36 31 31
-51 15 13 13
-40 31 28 27
-38 20 16 16

Figure 5: **Immunotherapy response prediction**. **a,** Evaluation for the prediction of durable response to immune checkpoint inhibitors (ICIs) across six cancer types and eight cohorts. ELF consistently outperforms existing models in AUC ($P < 0.05$). **b,** In non-small cell lung cancer, ELF generalizes well across both internal (Stanford) and external (CMB) validation cohorts. Left: ELF significantly outperforms baseline models in both cohorts ($P < 0.001$). Middle: Combining ELF risk scores with PD-L1 expression enhances predictive accuracy (AUC: 0.773±0.041), outperforming either alone. Right: Multivariable logistic regression confirms ELF as an independent predictor of ICI response after adjusting for clinical covariates including PD-L1 status and smoking history, $**$ $P < 0.01$, $*$ $P < 0.05$. **c,** In breast cancer, ELF shows good internal performance (neoadjuvant) and maintains strong predictive power in external validation (advanced). Left: Bar plots show AUCs across models ($P < 0.001$). Right: Two examples of advanced breast cancer cases with and without durable responses to immunotherapy (right panel). In this panel, the original WSIs, heatmaps, and two regions of interest (ROI) with high attention score were displayed from left to right, respectively. Distinct tumor morphology and immune/stromal infiltration were observed between the responding and non-responding cases. **d,** Kaplan–Meier analyses demonstrate that ELF-derived risk scores stratify progression-free survival (PFS) in three ICI-treated cohorts: lung (Stanford), gastroesophageal, and metastatic melanoma. Survival differences between high- and low-risk groups were assessed by a two-sided log-rank test. In **a**-**c**, all bar plots represent the mean and standard error based on five-fold cross-validation results or external validation results (using the bootstrap method with 1,000 replicates). The two-sided Wilcoxon signed-rank test was used to assess the statistical significance between ELF and other comparisons.

foundation models and the ensemble strategy on lung and breast external cohorts, where these performances confirmed the effectiveness of the ensemble strategy (**Extened Data Figure 8**).

Kaplan–Meier analysis showed that the ELF-derived risk score robustly stratifies PFS across nine cohorts (**Figure 5d** and **Extended Data Figure 9**). In three larger cohorts (lung (Stanford), gastroesophgeal, and metastatic melanoma), ELF effectively separated patients into high- and low-risk groups with hazard ratios (HRs) of 1.61 (95% CI: 1.11–2.34), 2.39 (1.43–3.98) and 2.27 (1.17–4.41), respectively (all $P < 0.05$). The median PFS were 5.1 *vs* 12.4 months, 4.8 *vs* 16.7 months and 10.3 *vs* 23.1 months for the high- and low-risk groups, respectively (**Figure 5d**). Consistent survival stratification was also seen in kidney (6.4 *vs* 19.8 months; HR 1.95 (1.01–3.76); $P = 0.0442$), head and neck (3.2 *vs* 11.0 months; HR 2.73 (1.43–5.18); $P = 0.0015$), localized bladder (4.0 *vs* 22.5 months; HR 4.84 (2.00–11.70); $P = 0.0001$), breast advanced (4.1 *vs* 13.7 months; HR 2.29 (1.05–4.98); $P = 0.0317$) and endometrial (6.0 *vs* 15.2 months; HR 1.81 (1.02–3.21); $P = 0.0413$). A similar trend was observed (5.3 *vs* 12.9 months) in advanced bladder cancer, although the result did not reach statistical significance (HR 1.86 (0.95–3.63); $P = 0.065$) given the small cohort size (**Extended Data Figure 9**). Together, these analyses demonstrate that an ELF score, derived from routine H&E images, consistently stratifies PFS across diverse tumour types and treatment settings.

To provide interpretability for the ELF model predictions, we performed attention-based visualization to identify the important regions for predicting immunotherapy response. Specifically, we overlaid ELF's attention maps on representative images and compared morphological patterns between responders and non-responders (**Figure 5c**, right panel and **Extended Data Figure 10**). In responder cases from both breast cancer

cohorts, the model's high-attention regions correspond to syncytial tumour cell nests with marked nuclear pleomorphism and dense intra- and peri-tumoural lymphoid infiltrates. By contrast, in non-responders, the high-attention areas were dominated by densely collagenized stroma with scant lymphocytic presence. Similarly, in the head and neck cohort, high-attention regions in responders highlighted brisk T-cell aggregates intermingled with pleomorphic tumour cells, whereas non-responder heat maps focused on acellular desmoplastic stroma devoid of inflammatory cells. These findings confirm that the ELF model's attention consistently focuses on immune-rich versus fibrotic regions that have been previously implicated in immune checkpoint-blockade efficacy[51].

Discussion

In this study, we introduce a novel paradigm for developing pathology foundation models, ELF, that harnesses the complementary representational strengths of independently trained foundation models. By employing an ensemble learning approach, ELF integrates five state-of-the-art foundation models through a unified slide-level encoder, enabling the generation of more robust and generalizable features. Evaluated across 115 diverse tasks—including disease subtyping, biomarker detection, and response prediction for both targeted therapies and immunotherapies—ELF consistently outperformed individual foundation models as well as existing slide-level approaches. These findings underscore the power of leveraging model complementarity and demonstrate the effectiveness of ensemble-based integration of pathology foundation models for improving performance in real-world clinical settings.

Most existing pathology foundation models are trained as tile-level models. For downstream applications, separate models must be trained to combine features from all the tiles in a slide. And since each whole-slide image (WSI) may contain thousands of tiles, this requires a large labeled dataset for training purposes. By contrast, ELF is a pretrained slide-level foundation model that directly encodes the entire WSI into compact representations. This has significant advantages over traditional tile-level foundation models by substantially reducing the need for training data, and therefore, is well suited to clinical contexts where data are limited. Indeed, we have shown that ELF could be fine-tuned using as few as 32 patients for therapeutic response prediction.

Although several slide-level foundation models have been developed[5,6,22], they are tightly coupled to one specific tile-level model[5,9,52]. Compared with these existing slide-level models, ELF improved the AUC by 9-14% for predicting anti-cancer therapy response; and by 10-17% for predicting immunotherapy response across all evaluation datasets. This improvement is attributable to the ensemble strategy of ELF that leverages the complementary strengths of the diverse set of pretrained foundation models that exist today. It is straightforward to further extend ELF to incorporate additional foundation models, although this will come at

increased computational cost.

Earlier efforts to combine multiple foundation models have not been particularly fruitful. One recent study[19] employed model distillation to learn from the knowledge of several expert models for a new tile-level foundation model. By smoothing out the differences across models, this approach does not fully exploit inter-model complementarity, and did not outperform existing foundation models in benchmark studies[20]. In another study[53], several models were used to learn tile-level weighting scores, however, feature extraction was performed using only a single foundation model (Virchow2[23]) . By contrast, ELF maintains the expressiveness of each foundation model by processing them independently and aligns their outputs through a shared slide encoder. This design allows ELF to preserve model-specific representations learned from their proprietary datasets and to integrate them synergistically. Empirical analyses revealed low correlation among the image features and attention maps generated from different base models. By aligning and combining these diverse features, ELF constructs richer slide-level representations that enhance predictive performance across diverse clinical applications.

The ability to detect therapeutically relevant biomarkers using routine H&E-stained slides has important implications for targeted therapies. This may facilitate rapid treatment decisions and potentially avoid unnecessary molecular testing. When evaluated on detecting 28 clinically actionable genetic alterations across 13 cancer types, ELF surpassed state-of-the-art foundation models with AUC exceeding 0.85 for specific gene mutations such as *BRAF* in thyroid carcinoma and *KRAS* in lung adenocarcinoma. The model maintains generalizability across diverse patient populations for detecting *BRAF*, *KRAS* mutations, and MSI status in colorectal cancer. In addition to individual genes, ELF can also accurately detect whole-genome doubling, tumor mutational burden and high aneuploidy, which are broadly shared tumor cell traits with significant prognostic implications and for which therapeutic targeting is currently under development[27,34,35].

Beyond detecting known biomarkers, we further evaluated ELF for predicting therapeutic responses and outcomes directly from pre-treatment H&E slides. Compared with existing pathology foundation models, ELF achieved superior predictive performance in various cancer types treated with a range of anticancer therapies including cytotoxic chemotherapy, molecularly targeted therapy, and immunotherapy. ELF's ability to generalize across tumor types, treatment modalities, and patient cohorts underscores its potential as a versatile treatment decision-support tool, especially in settings where data sparsity represents a major challenge for traditional models.

Although ELF demonstrated promising performance for therapy response prediction using H&E-stained slides, this alone may not be sufficient to guide treatment decisions. Incorporating other data modalities may further enhance predictive performance and clinical applicability. Indeed, we showed that combining the H&E-

based ELF model with simple immunohistochemistry markers such as CD8 or PD-L1 can significantly enhance the accuracy for predicting neoadjuvant therapy response in breast cancer and immunotherapy response in lung cancer. Integration with additional multimodal data such as clinical reports, radiology images, and genetic alterations may warrant further investigation[7,44,54]. While ELF has been evaluated across multiple cancer types and therapies, much of the evidence comes from retrospective, single-institution cohorts. Future prospective trials in diverse patient populations will be essential to validate these findings and facilitate the translation of ELF into a practical clinical tool.

In conclusion, this study introduces a new paradigm for building foundation models, one that shifts the focus from constructing ever-larger models to strategically integrating the complementary strengths of existing pretrained models. Our ensemble learning-based approach enables the creation of robust and generalizable representations without requiring access to proprietary training data. The resulting ensemble foundation model demonstrates superior performance in challenging disease classification, biomarker detection, and response prediction for anticancer therapies and immunotherapy across a wide range of cancers. Together, these findings suggest ELF as a next-generation AI tool for precision oncology.

Methods

Data curation for pretraining

For pretraining of the ELF foundation model, we collected 53,699 whole-slide images (WSIs) and their corresponding clinical information (such as tissue of origin and tissue type: cancer vs normal) from 11 publicly available datasets, including ACROBAT[55], BCNB[56], COBRA[57], DHMC[58,59], GETx[60], IMP-CRS[61,62], IPD-Brain[63], NMI-Bladder[64], PAIP[65], PANDA[66], TCGA[29]. In the TCGA, we only used four cohorts: TCGA-THCA, TCGA-CESC, TCGA-ESCA, and TCGA-UCEC, since these anatomical sites are not represented in the other public datasets. All images of this training set are formalin-fixed paraffin-embedded tissues stained with haematoxylin and eosin (H&E) and come from 20 anatomic sites including adrenal, bladder, brain, breast, cervical, colorectal, esophagus, heart, kidney, liver, lung, ovary, pancreas, prostate, skin, stool, stomach, testis, thyroid, and uterus. **Figure 1b** presents an overview of the data distribution across these anatomic sites. Detailed data distribution is summarized in **Extended Data Table 1**.

Model design and pretraining

To harness the complementary strengths of multiple pathology foundation models, we developed ELF (Ensemble Learning of Foundation models), a unified slide-level ensemble framework. Instead of directly concatenating high-dimensional features from different models—which typically demands large-scale labelled data for training the multiple-instance classifier and may introduce training instability—ELF integrates information from multiple foundation models through a compact, learnable architecture. Specifically, it employs a multi–head attention–based multi-instance learning model as a patch aggregator[67], trained using a combination of contrastive learning and weakly supervised learning. This enables ELF to generate a robust and generalized slide-level representation. The overall pipeline for ELF pertaining is shown in **Figure 1a**.

In the ELF framework, each WSI is encoded into a unified slide-level representation through three main steps: (1) tissue segmentation and patching; (2) patch-level feature embedding using five pretrained pathology foundation models; (3) patch feature aggregation and ensemble representation synthesis. For tissue segmentation and patching, we used the CLAM toolbox[68] to extract non-overlapping patches of size 1024 $\times$ 1024, 512 $\times$ 512 or 256 $\times$ 256 pixels at 40$\times$, 20$\times$ or 10$\times$ magnification (~0.25 um/pixel, ~0.50 um/pixel or ~1.0 um/pixel) and resize to a patch size suitable for each of the tile-level foundation models. To capture diverse morphological patterns, patch-level features were extracted using five state-of-the-art foundation models with their default settings: UNI[10], CONCHV1.5[9], GigaPath[5], H-optimus-0[8], and Virchow2[23]. These models are pretrained on distinct large-scale pathology datasets and have demonstrated strong performance in downstream tasks[7,69]. These heterogeneous embeddings were then fed into a unified ensemble architecture, which employs

attention-based multiple instance learning to independently encode each set of features and integrate them into a compact slide-level representation that leverages the complementary value of the constituent models.

Slide encoder. ELF employs the attention-based multiple instance learning (AbMIL) model[67,68] with multiple attention heads as a backbone[6,53,70]. For preprocessing, input patch embeddings from different foundation models with varying dimensions ($X \in \{\mathbb{R}^{N\times 768}, \mathbb{R}^{N\times 1024}, \mathbb{R}^{N\times 1280}, \mathbb{R}^{N\times 1536}\}$) are dynamically resized to a unified dimensional space ($X^{768} \in \mathbb{R}^{N\times 768}$) using linear interpolation, which ensures consistent feature representation across different patch encoders. Then, they are normalized with a LayerNorm layer before the attention computation.

The slide encoder architecture utilizes a fixed 8-head attention mechanism where input features $X^{768} \in \mathbb{R}^{N\times 768}$ are reshaped into $\mathbb{R}^{N\times 96\times 8}$, with each attention head processing 96-dimensional feature slices independently. Each head employs a separate AbMIL network with hidden dimensions of 96, following the gated attention formulation with two parallel branches (a and b). The attention weights α_i for each head i are computed as:

$$\alpha_i = c_i(\tanh(a_i X_i^{768}) \odot \sigma(b_i X_i^{768})) \tag{1}$$

where $\odot$ denotes element-wise multiplication, tanh and σ represent the hyperbolic tangent and sigmoid functions, respectively, and X_i^{768} represents the feature slice for head i. The individual attention scores from all 8 heads are aggregated by averaging across the head dimension, followed by transpose and softmax normalization. The final slide-level features are computed by weighted aggregation using both processed and original features.

$$s_i^{768} = \text{softmax}(\bar{\alpha})^T X_i^{768}, \quad s_i = \text{softmax}(\bar{\alpha})^T X_i \tag{2}$$

where $\bar{\alpha}$ represents the mean-aggregated attention weights across all 8 heads, s_i^{768} denotes the processed slide embedding with unified 768 dimensions, and s_i represents the raw slide embedding that preserves the original patch encoder dimensions. A unified dimension for slide embeddings facilitates model training, while s_i maintains the native characteristics of different foundation models, which enables consistent attention computation and leverages model-specific feature representations. These slide embeddings are fused by concatenation as the final slide representation.

Contrastive pretraining. We trained ELF with the momentum contrastive learning framework (MoCoV3)[16], which consists of a base encoder and a momentum encoder to learn discriminative slide-level representations. The momentum encoder parameters θ_k are updated using exponential moving averages of the base encoder parameters θ_q:

$$\theta_k \leftarrow m\theta_k + (1-m)\theta_q \tag{3}$$

where $m \in [0,1)$ denotes the momentum coefficient set to 0.99.

For positive pair construction, we employ two complementary strategies to capture both cross-foundation models consistency and different views coherence. First, we treat embeddings extracted from the same tissue region using different foundation models as positive pairs, enabling the model to learn model-invariant representations across different foundation models. Second, we construct a positive pair with two tissue regions with overlap, which were processed by the same foundation model, encouraging cross-view consistency within the embedding space. This dual positive sampling strategy ensures that the learned attention representations capture both cross-foundation models alignment and cross-view relationships inherent in histopathological structures.

The contrastive loss follows the InfoNCE formulation[71], where for a given query q, the objective maximizes agreement with its corresponding positive key k^+ while minimizing similarity to negative samples:

$$\mathcal{L}_{cont} = -\log \frac{\exp(\text{sim}(q,k^+)/\tau)}{\sum_{i=1}^{N} \exp(\text{sim}(q,k_i)/\tau)} \tag{4}$$

where $\text{sim}(\cdot,\cdot)$ denotes cosine similarity, $\tau = 0.2$ is the temperature parameter, and N represents the batch size. To prevent representational collapse, queries and keys are generated by distinct encoders with the momentum-updated key encoder providing more stable targets during training.

Weakly-supervised pretraining. We further incorporated weakly supervised signals through auxiliary classification tasks that leverage readily available clinical metadata. Specifically, we employed two classification heads: a binary cancer classification head that distinguishes between cancer and non-cancer samples, and a multi-class organ classification head that predicts the anatomical tissue of origin across 20 different organs. The combined classification loss is formulated as:

$$\mathcal{L}_{cls} = \frac{1}{4}[\mathcal{L}_{CE}(p_1^{cancer}, y^{cancer}) + \mathcal{L}_{CE}(p_2^{cancer}, y^{cancer}) + \mathcal{L}_{CE}(p_1^{organ}, y^{organ}) + \mathcal{L}_{CE}(p_2^{organ}, y^{organ})] \tag{5}$$

where $\mathcal{L}_{CE}$ denotes cross-entropy loss, p_i represents the predictions from the i-th augmented view, and y denotes the corresponding ground truth labels. This weakly supervised approach provides semantic guidance during representation learning while requiring only coarse-grained annotations that are routinely collected in clinical practice. The total training objective combines both contrastive and classification losses:

$$\mathcal{L}_{total} = \mathcal{L}_{cont} + \lambda \mathcal{L}_{cls} \tag{6}$$

where λ balances the contribution of supervised and self-supervised components. This hybrid training strategy enables the model to learn both semantically meaningful and discriminative representations suitable for diverse downstream tasks.

Pretraining settings. We pretrained ELF with 53,699 WSIs (90% for training and 10% for validation, **Extended Data Table 1**) and the combination objective function $\mathcal{L}_{total}$ for 300 epochs using distributed training across 8 NVIDIA H100 GPUs with a total effective batch size of 768 samples. Each sample consisted of up to 4,096 patch embeddings extracted from different foundation models (CONCHV1.5[10], GigaPath[5], H-Optimus-0[8], UNI[9], and Virchow2[23]), with feature dimensions varying from 768 to 1,536 depending on the patch encoder architecture. The training employed the AdamW optimizer with $\beta_1 = 0.9$, $\beta_2 = 0.95$, and $\varepsilon = 1 \times 10^{-8}$. We implemented a cosine learning rate decay scheduler with a peak learning rate of 1×10^{-4}, linear warm-up over 10 epochs, and weight decay of 0.05. The momentum coefficient for the key encoder was dynamically adjusted using a cosine schedule from 0.996 to 0.999 throughout training. Mixed-precision training with automatic mixed precision (AMP) was employed to reduce memory consumption and accelerate training while maintaining numerical stability. The total loss combined contrastive and classification objectives with equal weighting (λ=1). We validated the trained model every 2 epochs and selected the highest-performing checkpoint across tissue of origin and cancer vs normal classification for downstream tasks.

Model evaluation and datasets

We evaluated the effectiveness and generalizability of the pretrained ELF model on four major clinical applications in oncology: disease classification and subtyping, therapeutic biomarker detection, anticancer therapy response prediction, and immunotherapy response prediction. As in prior work[22,70], we adopted a linear probing strategy (logistic regression)[17] for all downstream tasks. Besides, we also evaluated the performance of ELF in regression tasks using XGB[72] with the same linear probing strategy. In all evaluation experiments, data were split either based on label stratification or according to the official dataset partitions. Each WSI was encoded into a slide embedding using the pretrained ELF slide encoder. For comparison, we benchmarked ELF against three state-of-the-art slide-level foundation models (CHIEF[6], Prov-GigaPath[5], and TITAN[22]) under the same evaluation settings.

Disease classification and subtyping. We first evaluated ELF's performance on disease classification and subtyping tasks based on WSIs. To evaluate its generalizability across different organs and subtyping complexities, we used three large-scale publicly available benchmark datasets: the Basal Cell Carcinoma Classification dataset (BCCC; skin cancer, 2 /3 /5 cls, cla means class), the BReAst Carcinoma Subtyping dataset (BRACS; breast cancer, 7 cls), and the EBRAINS dataset (brain tumors, 12/30 cls). All evaluations followed the official data splits provided by the original studies. Detailed data distribution was represented in **Extended Data Table 2**. The details of each dataset and evaluation are described below.

BCCC. This dataset consists of 1,832 WSIs from excision specimens of cutaneous basal cell carcinomas collected at the Department of Pathology at Sahlgrenska University Hospital[24]. It has three different

classification tasks (binary, three, and five classes). The official split includes training and testing sets with 1,435 and 397 WSIs, respectively. One WSI was removed from the training set due to its low image quality. We conducted five-fold cross-validation on the training set and ensembled their prediction on the testing set as final predictions.

BRACS. This is a breast carcinoma subtyping dataset with 6 different subtypes of lesions (including pathological benign, usual ductal hyperplasia, flat epithelial atypia, atypical ductal hyperplasia, ductal carcinoma in situ, and invasive carcinoma) and normal tissue samples (7 cls totally)[25]. A total of 547 WSIs is split into training, validation, and testing sets with 395, 65, and 87 WSIs, respectively.

EBRAINS. This is an established brain tumor subtyping dataset for pathology model evaluation[26]. It includes 2,319 WSIs with coarse (12 cls) and fine-grained (30 cls) classification labels. The dataset is split[9,22,70] into training, validation, and testing sets with 1,151, 595, and 573 WSIs, respectively.

Molecular biomarker detection. To evaluate ELF's capacity to predict clinically relevant molecular biomarkers from histopathology slides, we performed a comprehensive assessment across multiple biomarkers and cancer types. Specifically, we evaluated ELF on (1) 74 binary biomarker classification tasks from The Cancer Genome Atlas (TCGA); (2) three key biomarkers (*BRAF*/*KRAS* mutations and MSI status) across three independent colorectal cancer (CRC) cohorts to test generalizability; and (3) a pan-cancer aneuploidy score regression task; (4) whole genome doubling classification task and (5) tumor mutational burden classification task to evaluate ELF's ability to capture chromosomal instability–related morphological patterns. In all experiments, we compared ELF with state-of-the-art slide-level foundation models (CHIEF[6], Prov-GigaPath[5], and TITAN[22]) under the same evaluation settings.

TCGA biomarkers. We assessed ELF's ability to predict a broad panel of therapeutic biomarkers across cancers in TCGA dataset. We started from 54 candidate biomarkers[73] curated from My Cancer Genome (MCG)[74] and OncoKB [29,75], where some of them are associated with a clinically proven targeted therapy and others are recommended by the National Comprehensive Cancer Network (NCCN). We then applied a minimum threshold of five altered cases per biomarker–cancer pair to ensure statistical robustness. This filtering yielded a final evaluation set of 28 biomarkers across 13 cancer types, comprising 7,721 WSIs from 6,510 patients (**Extended Data Table 3**). The included cancer types were BLCA, BRCA, CRC (COAD and READ), ESCA, LGG/GBM, LIHC, LUAD/LUSC, OV, PAAD, PRAD, SKCM, THCA, and UCEC. The biomarker panel consist of *AKT1, ATM, BARD1, BRAF, BRCA1, BRCA2, CCND1, CDK4, CHEK2, EGFR, ERBB2, ESR1, FGFR2, FGFR3, IDH1, KIT, KRAS, MET, MLH1, NBN, NRAS, PIK3CA, POLE, PTEN, ROS1, TP53, TSC1*, and *TSC2*. The performance of ELF for each biomarker was assessed via five-fold cross validation under the linear probing settings, with stratified sampling by alteration status.

***BRAF*, *KRAS*, and MSI biomarkers in CRC.** To further evaluate ELF's generalizability in clinically actionable biomarker prediction, we focused on three key biomarkers (*BRAF/KRAS* mutations and MSI status), across four large colorectal cancer (CRC) cohorts, totaling 2,711 patients. These included the Molecular and Cellular Oncology study (MCO)[31,32] (1,490 patients), SR386[30] (400 patients), SR1482[30] (399 patients), and TCGA-CRC[29] (501 patients) cohorts. SR386 (primary CRC) as a recently released real-world data was used as the internal development cohort with five-fold cross-validation to train five independent models. These models were then applied to the three external validation cohorts: SR1482 (metastatic and primary CRC), MCO (archival resection cases from 1994–2010), and TCGA-CRC (primary CRC with genomic characterizations). For each external WSI, the final prediction was averaged across the five models. Detailed cohort statistics are provided in **Extended Data Table 4**.

Aneuploidy regression. We applied the ELF model to predict the continuous Aneuploidy Score from routine histopathology images. We evaluated the performance using the TCGA pan-cancer dataset, which included a total of 8,819 patients and 10,854 WSIs. All patients were split into training, validation, and test sets at a ratio of 7:1:2. For this regression task, we used three metrics to evaluate performance, including Pearson correlation, Mean Squared Error, and Coefficient of determination (R^2). Detailed data distribution was represented in **Extended Data Table 5**.

Whole genome doubling classification. We also applied the ELF model to classify the whole genome doubling (WGD) from routine histopathology images[27]. We evaluated the performance using the TCGA pan-cancer dataset with the same data split as the Aneuploidy regression task. We simplified this task as the prediction of WGD positive (includes samples with 1 or 2 WGD) versus WGD negative (0 WGD) like the existing clinical study[27]. Detailed data distribution was represented in **Extended Data Table 6**.

Tumor mutational burden classification. We further used the ELF model to classify the tumor mutational burden (TMB) from routine histopathology images[27]. We simplified this task as the positive versus negative prediction using the clinically recommended cutoff with 10 mut/Mb[27]. We evaluated the performance using the TCGA pan-cancer dataset through cross-validation, as the total number of positive patients is too limited. Detailed data distribution was represented in **Extended Data Table 6**.

Model visualization

To enhance interpretability of the model, we visualized attention maps to highlight the spatial regions driving the ELF predictions. First, WSIs were tiled with 80% overlap to produce a fine-grained scalar attention weight. Raw scores were min–max normalized to the [0, 1] and mapped to a continuous colormap and composited over the original high-resolution WSI with a semi-transparent overlay, so that warmer hues pinpoint the most

influential regions for model prediction.

Statistical analysis

We used the balanced accuracy (BA) to evaluate the performance of disease classification and subtyping. For tasks with an independent testing set, we assessed performance variations with the non-parametric bootstrapping method and obtained 95% confidence intervals (CIs) from 1000 bootstrap samples. We used the area under the curve (AUC) to evaluate the performance of biomarker detection as well as prediction of anticancer therapy response and immunotherapy response. For regression tasks, we used the Pearson correlation, mean squared error (MSE), and coefficient of determination (R^2) to measure the model performance. For tasks without an independent testing set, the performance variations were evaluated by standard error across five-fold cross validation. Statistical significance analyses were conducted using a two-sided Wilcoxon signed-rank test. Kaplan–Meier curves were used to visualize the patient stratification and the log-rank test used for comparing different risk groups, with the median predicted probability as the cut-off value.

Inclusion and Ethics Statement

The study was approved by the Institutional Review Board of Stanford University (protocol #67432). Informed consent was waived for this retrospective analysis.

Computing hardware and software

We used Python (version 3.10.12), PyTorch (version 2.6.0, CUDA 12.4) (`https://pytorch.org`) and other necessary open-source packages for all experiments and analyses. For pretraining, we employed 8 $\times$ 80G NVIDIA H00 GPUs for multi-GPU and mixed-precision training using distributed data-parallel (DDP). We used OpenSlide (version 4.3.1), openslide-python (version 1.4.2) and CLAM[68] and their required packages to process all WSIs. All downstream experiments were conducted on a cluster server with 8 $\times$ 48G NVIDIA L40 GPUs. We used several public machine learning packages for linear prob evaluation, analysis and visualization, including Scikit-learn (version 1.6.1), Scikit-survival (version 0.24.0) and Matplotlib (version 3.10.0). We used five tile-level foundation models for feature extraction, these pretrained models are publicly accessible: UNI (`https://huggingface.co/MahmoodLab/UNI`), CONCHV1.5 (`https://huggingface.co/MahmoodLab/conchv1_5`), Gigapath (`https://huggingface.co/prov-gigapath/prov-gigapath`), Virchow2 (`https://huggingface.co/paige-ai/Virchow2`) and H-optimus-0 (`https://huggingface.co/bioptimus/H-optimus-0`). The implementations and pretrained models of comparison methods (slide encoders) were listed here: CHIEF (`https://github.com/hms-dbmi/CHIEF`), Prov-GigaPath (`https://huggingface.co/prov-gigapath/prov-gigapath`) and TITAN (`https://huggingface.co/MahmoodLab/TITAN`).

Data Availability

The histopathology images and clinical information used for pretraining are available at the following: ACROBAT (https://researchdata.se/en/catalogue/dataset/2022-190-1), BCNB (https://bupt-ai-cz.github.io/BCNB), COBRA (https://registry.opendata.aws/cobra), DHMC (https://bmirds.github.io/), GTEx (https://www.gtexportal.org/home), IMP-CRS (https://rdm.inesctec.pt/dataset/nis-2023-008), IPD-Brain (https://hai.iiit.ac.in/ipd), NMI-Bladder (https://figshare.com/projects/nmi-wsi-diagnosis/61973), PAIP (http://www.wisepaip.org/), PANDA (https://www.kaggle.com/c/prostate-cancer-grade-assessment/data) and TCGA (https://portal.gdc.cancer.gov). Disease subtyping datasets can be found at the listed links: BCCC (https://datahub.aida.scilifelab.se/10.23698/aida/bccc), BRACS (https://www.bracs.icar.cnr.it/), EBRAINS (10.25493/WQ48-ZGX). Biomarker datasets are available in the following links: MCO (https://www.sredhconsortium.org/sredh-datasets/mco-study-whole-slide-image-dataset) and SurGen (https://www.ebi.ac.uk/biostudies/studies/S-BIAD1285).

Code Availability

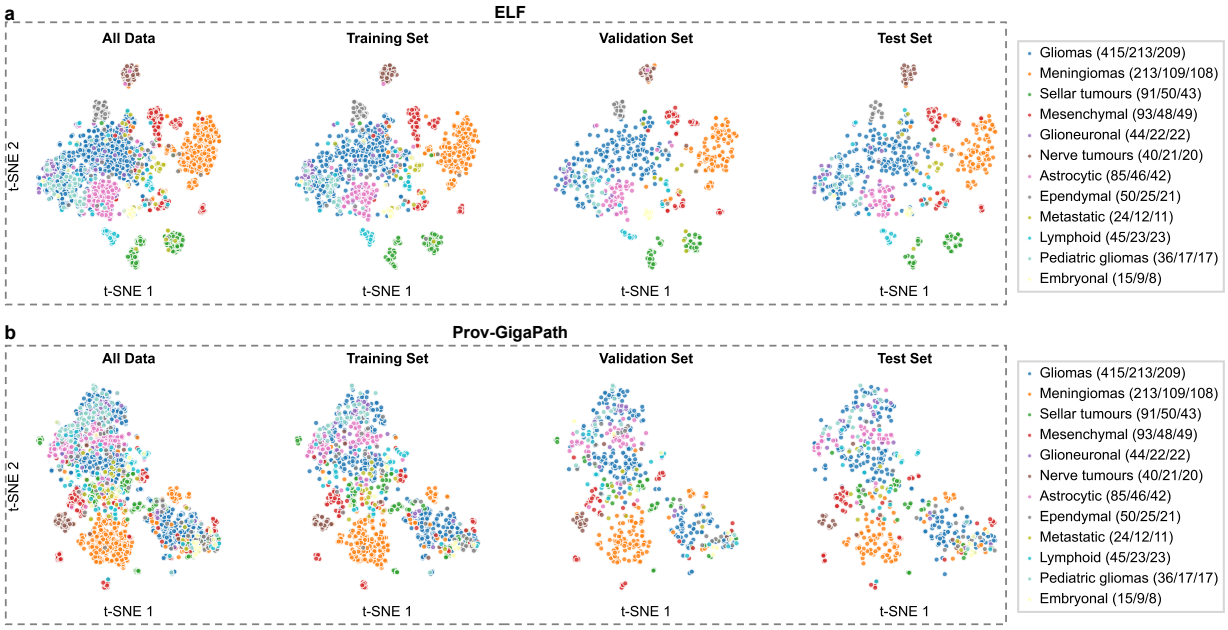
Our work is publicly available at https://github.com/lilab-stanford/ELF, including installation, model weights, and example data.

Competing interests

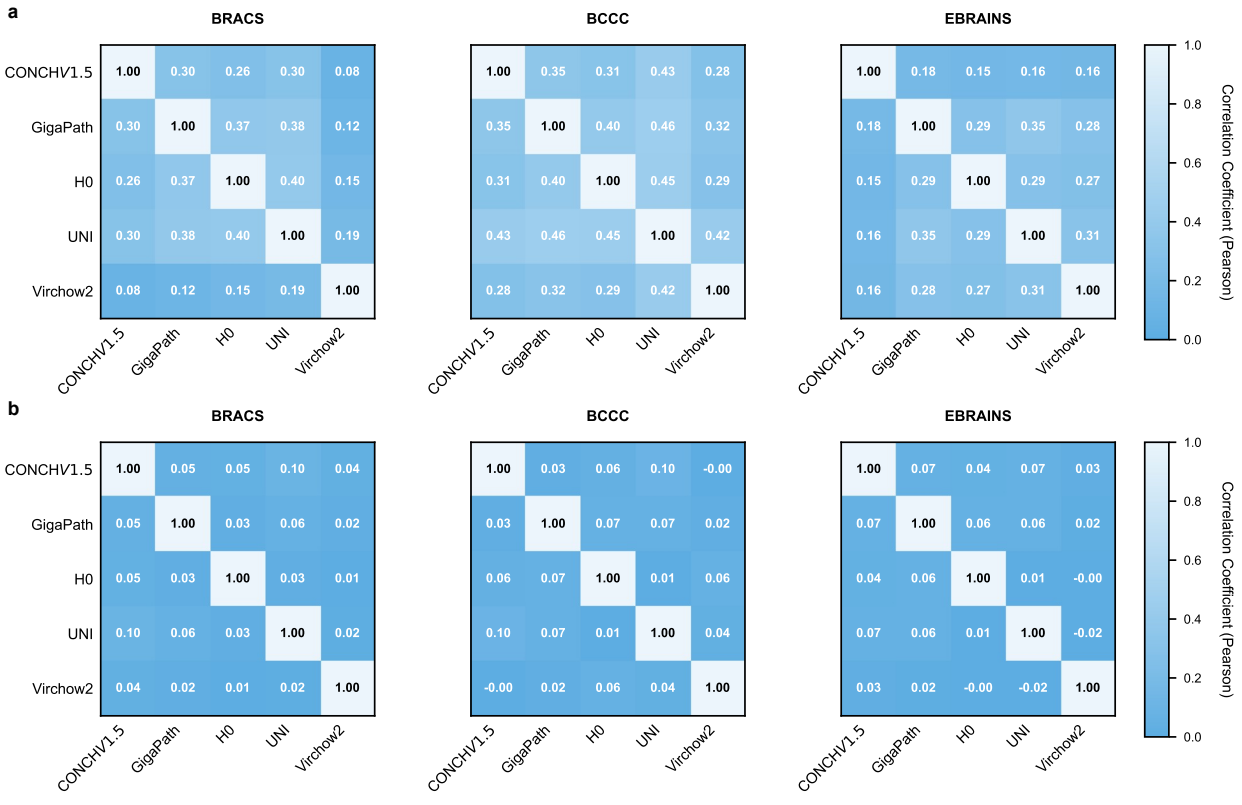
The authors declare no competing interests.

Acknowledgements

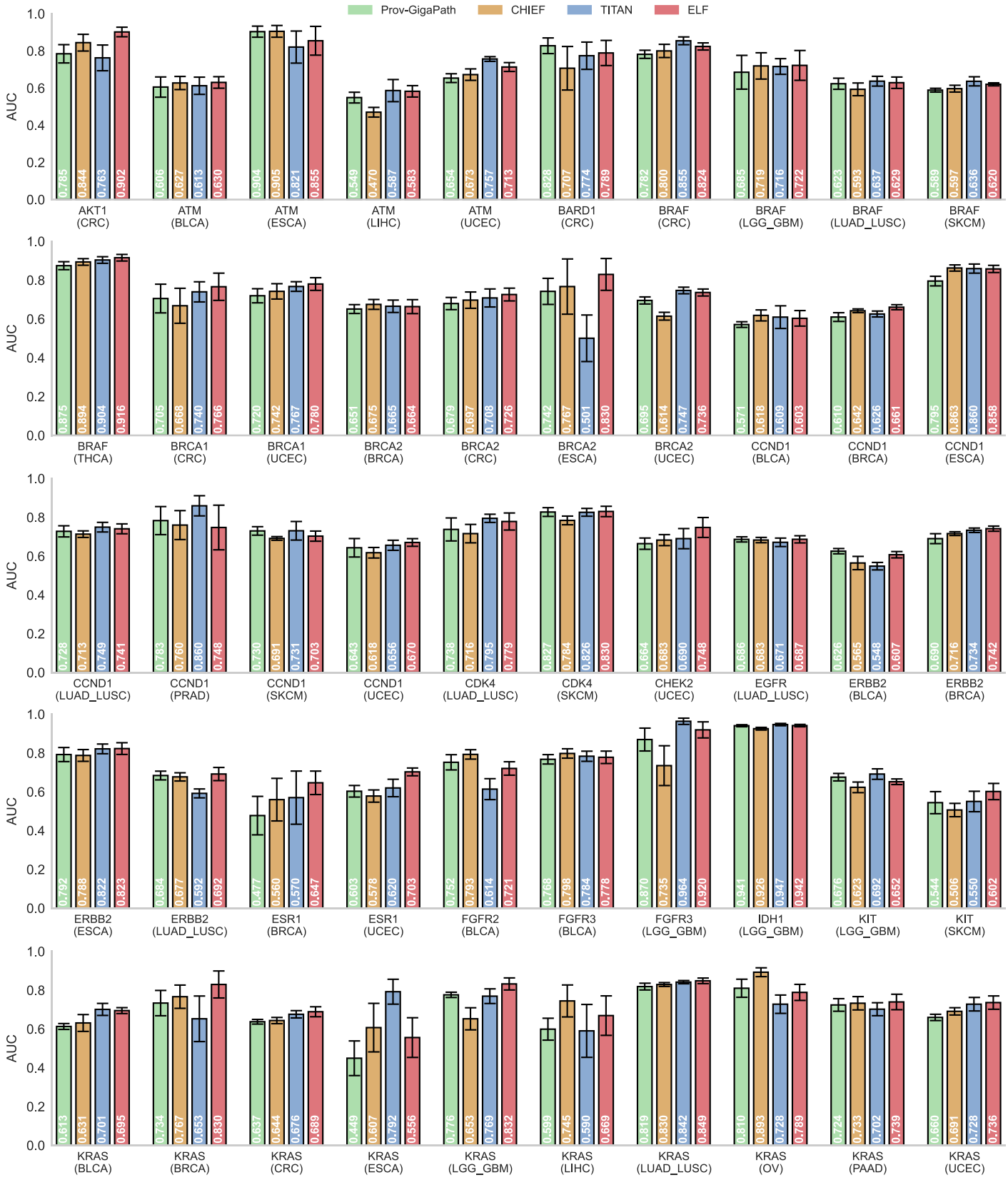
We acknowledge the ACROBAT[55], BCNB[56], COBRA[57], DHMC[58,59], GTEx[60], IMP-CRS[61,62], IPD-Brain[63], NMI-Bladder[64], PAIP[65], PANDA[66], TCGA[29], BCCC[24], BRACS[25], EBRAINS[26], MCO[31,32], SurGen[30]. In addition, we acknowledge the research team[27] for providing the aneuploidy scores and curating the whole-genome doubling (WGD) and tumor mutational burden data. We also thank our colleagues at Stanford Medicine[76] for their contributions to the immunotherapy patient cohort. We gratefully acknowledge the use of Marlowe, Stanford's GPU-based computational instrument, for computational support.

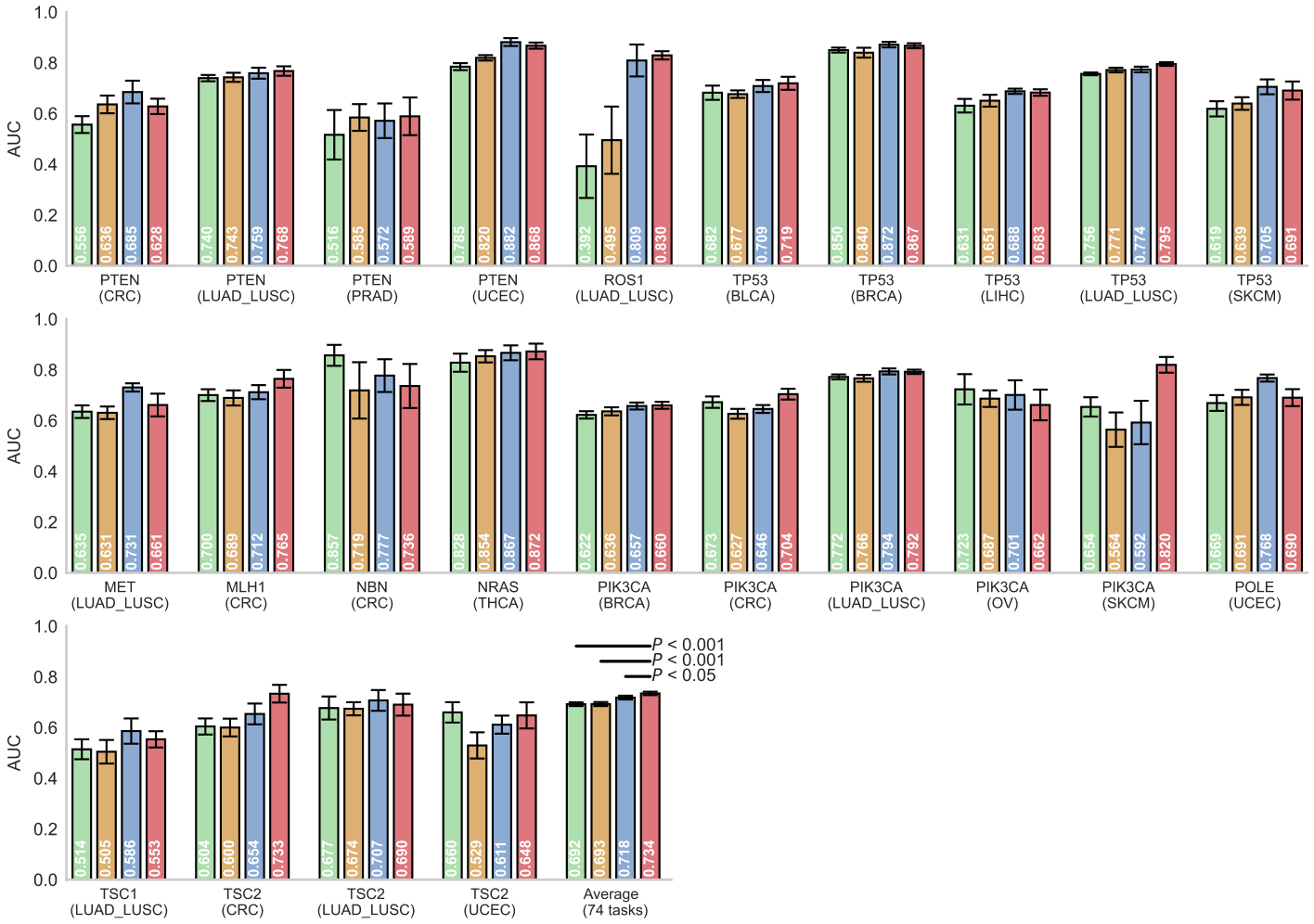


Extended Data Figure 1: **Comparison of clustering capability.** Detailed comparisons of the two-dimensional t-distributed stochastic neighbor embedding (t-SNE) representation in the EBRAINS (with 12 classes) training, validation, test cohorts and all patients between ELF (**a**) and Prov-GigaPath (**b**).

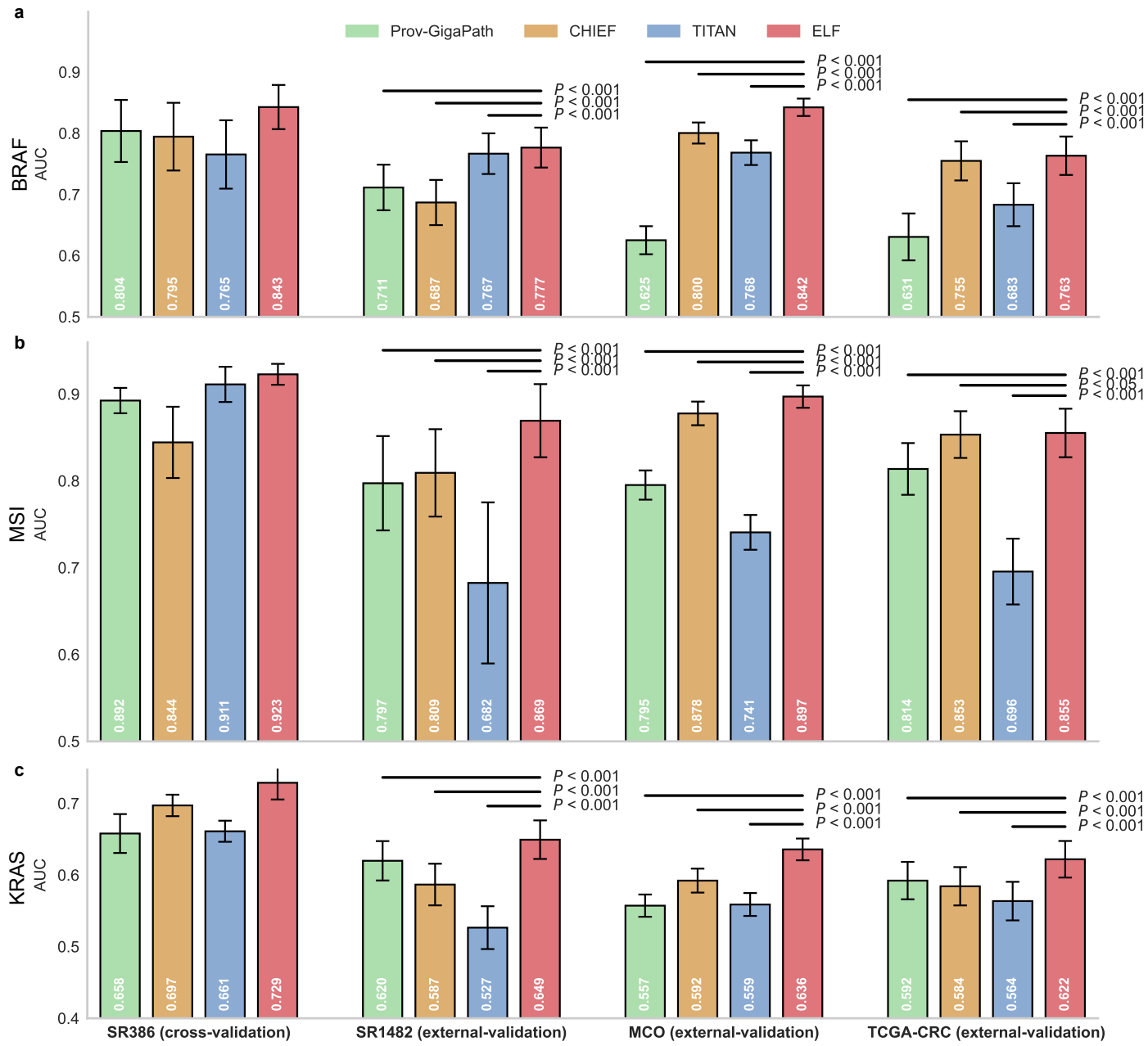


Extended Data Figure 2: **Pearson correlation analysis in attention scores and slide-level embeddings across foundation models.** **a,** Pearson correlation analysis of attention scores across different foundation models in three large-scale datasets. All attention scores obtained by the pretrained slide encoder in ELF. **b,** Pearson correlation analysis of slide embedddings across different foundation models in three large-scale datasets. We leveraged the pretrained slide encoder to generate 768-dimensional embeddings in a unified space for subsequent correlation analysis.

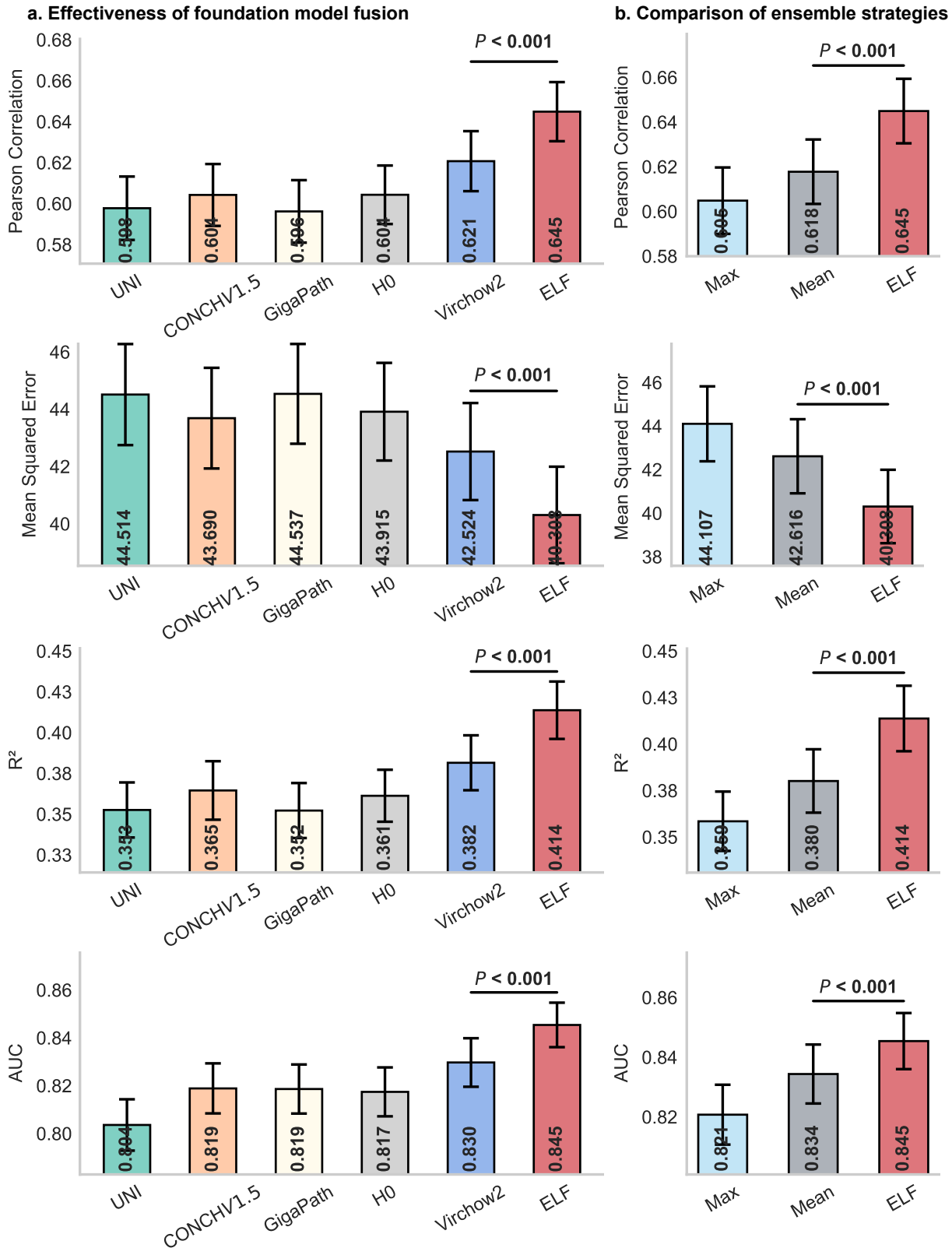

Prov-GigaPath
CHIEF
TITAN
ELF
AUC
AKT1 (CRC) 0.785 0.844 0.763 0.902
ATM (BLCA) 0.606 0.627 0.613 0.630
ATM (ESCA) 0.904 0.905 0.821 0.855
ATM (LIHC) 0.549 0.470 0.587 0.583
ATM (UCEC) 0.654 0.673 0.757 0.713
BARD1 (CRC) 0.828 0.707 0.774 0.789
BRAF (CRC) 0.782 0.800 0.855 0.824
BRAF (LGG_GBM) 0.685 0.719 0.716 0.722
BRAF (LUAD_LUSC) 0.623 0.593 0.637 0.629
BRAF (SKCM) 0.589 0.597 0.636 0.620
BRAF (THCA) 0.875 0.894 0.904 0.916
BRCA1 (CRC) 0.705 0.668 0.740 0.766
BRCA1 (UCEC) 0.720 0.742 0.767 0.780
BRCA2 (BRCA) 0.651 0.675 0.665 0.664
BRCA2 (CRC) 0.679 0.697 0.708 0.726
BRCA2 (ESCA) 0.742 0.767 0.501 0.830
BRCA2 (UCEC) 0.695 0.614 0.747 0.736
CCND1 (BLCA) 0.571 0.618 0.609 0.603
CCND1 (BRCA) 0.610 0.642 0.626 0.661
CCND1 (ESCA) 0.795 0.863 0.860 0.858
CCND1 (LUAD_LUSC) 0.728 0.713 0.749 0.741
CCND1 (PRAD) 0.783 0.760 0.860 0.748
CCND1 (SKCM) 0.730 0.691 0.731 0.703
CCND1 (UCEC) 0.643 0.618 0.656 0.670
CDK4 (LUAD_LUSC) 0.738 0.716 0.795 0.779
CDK4 (SKCM) 0.827 0.784 0.826 0.830
CHEK2 (UCEC) 0.664 0.683 0.690 0.748
EGFR (LUAD_LUSC) 0.686 0.683 0.671 0.687
ERBB2 (BLCA) 0.626 0.565 0.548 0.607
ERBB2 (BRCA) 0.690 0.716 0.734 0.742
ERBB2 (ESCA) 0.792 0.788 0.822 0.823
ERBB2 (LUAD_LUSC) 0.684 0.677 0.592 0.692
ESR1 (BRCA) 0.477 0.560 0.570 0.647
ESR1 (UCEC) 0.603 0.578 0.620 0.703
FGFR2 (BLCA) 0.752 0.793 0.614 0.721
FGFR3 (BLCA) 0.768 0.798 0.784 0.778
FGFR3 (LGG_GBM) 0.870 0.735 0.964 0.920
IDH1 (LGG_GBM) 0.941 0.926 0.947 0.942
KIT (LGG_GBM) 0.676 0.623 0.692 0.652
KIT (SKCM) 0.544 0.506 0.550 0.602
KRAS (BLCA) 0.613 0.631 0.701 0.695
KRAS (BRCA) 0.734 0.767 0.653 0.830
KRAS (CRC) 0.637 0.644 0.676 0.689
KRAS (ESCA) 0.449 0.607 0.792 0.556
KRAS (LGG_GBM) 0.776 0.653 0.769 0.832
KRAS (LIHC) 0.599 0.745 0.590 0.669
KRAS (LUAD_LUSC) 0.819 0.830 0.842 0.849
KRAS (OV) 0.810 0.893 0.728 0.789
KRAS (PAAD) 0.724 0.733 0.702 0.739
KRAS (UCEC) 0.660 0.691 0.728 0.736



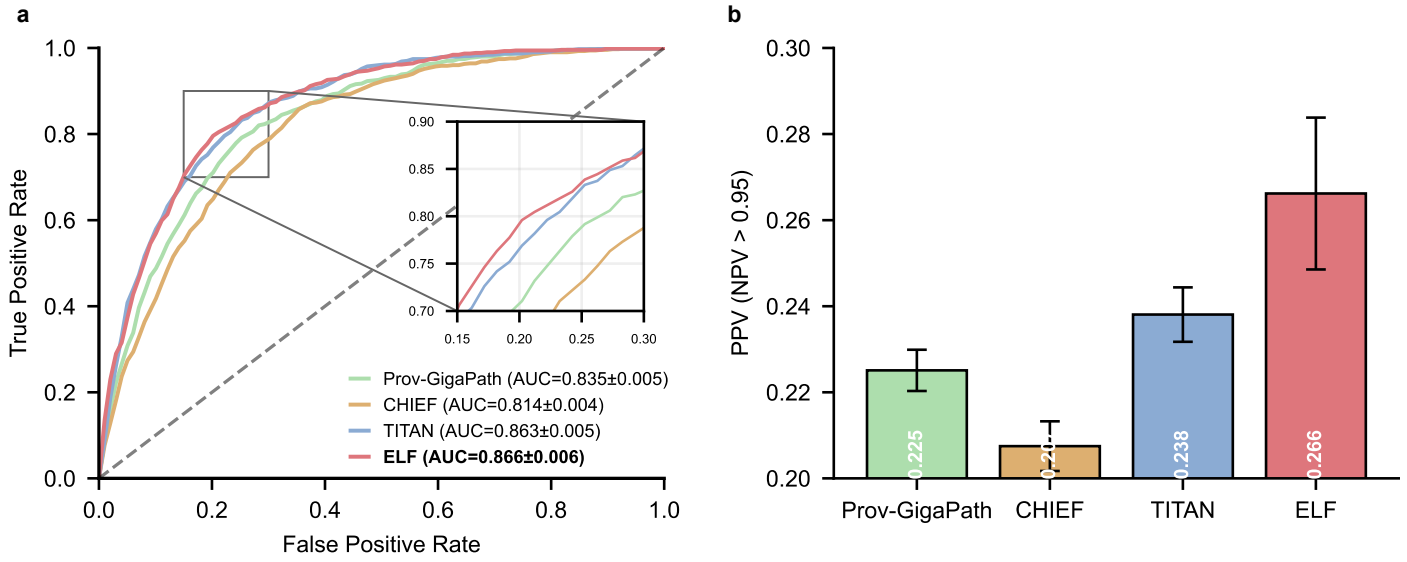
Extended Data Figure 3: **Detailed performance comparison of biomarker prediction in the TCGA dataset between ELF and others.** Results are reported as mean ± standard error over five-fold cross-validation, and statistical significance was determined using two-sided Wilcoxon signed-rank tests.



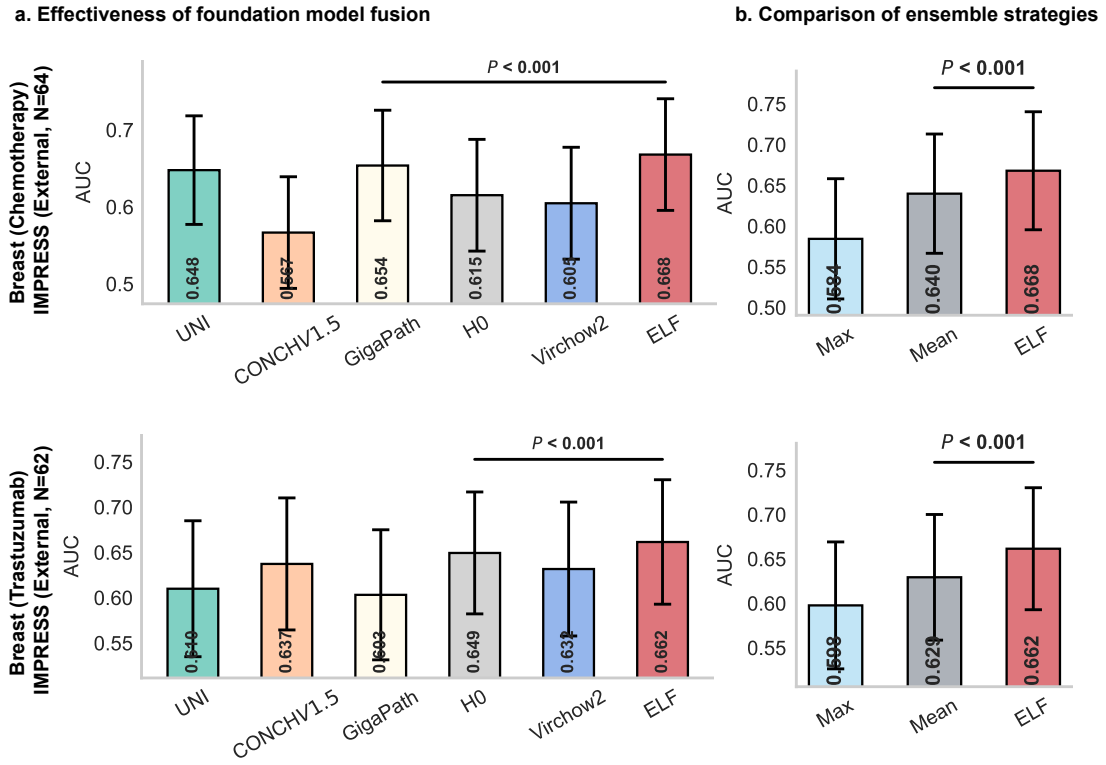
Extended Data Figure 4: **Detailed performance comparison of biomarker prediction in CRC cohorts between ELF and others. a, b** and **c** presented the performance of BRAF, MSI and KRAS status predictions, respectively. The error bars represent the mean and standard error based on five-fold cross-validation results or external validation results (using the bootstrap method with 1,000 replicates). The two-sided Wilcoxon signed-rank test was used to assess the statistical significance between ELF and other comparisons.



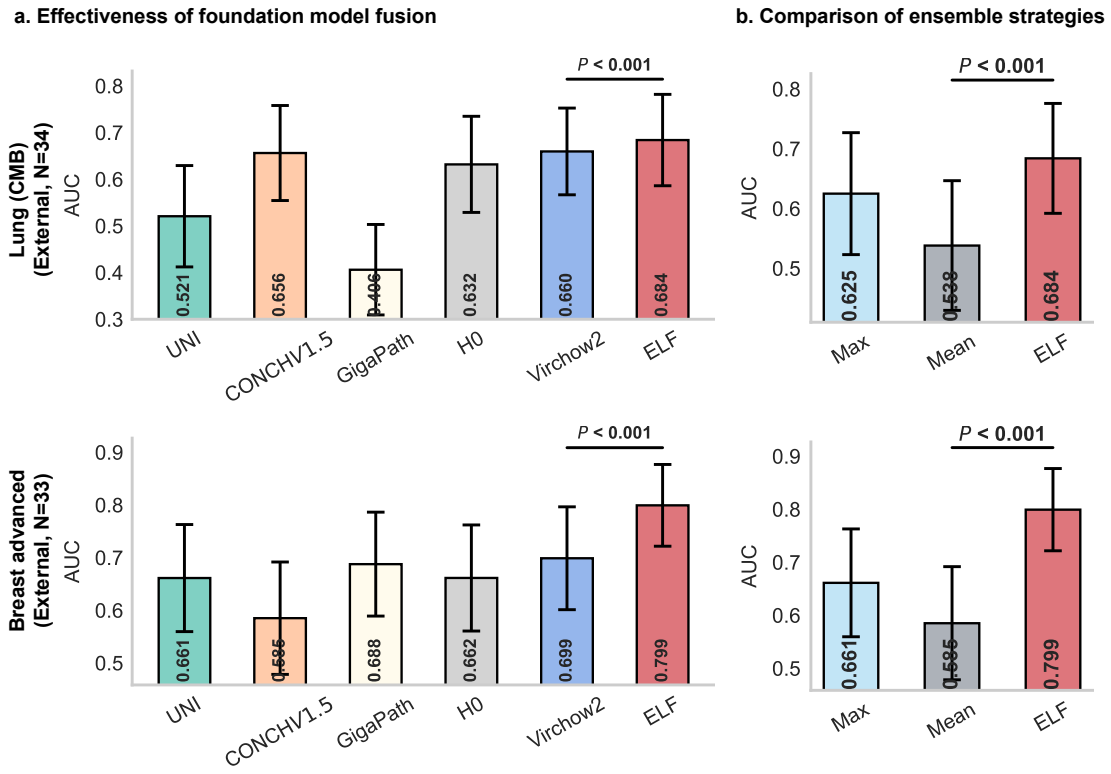
Extended Data Figure 5: **The performance of integrations of diverse foundation models and the ensemble strategy on the aneuploidy score regression and WGD classification tasks. a,** ELF significantly outperformed individual foundation models both on the regression and classification tasks across four metrics ($P < 0.001$), confirming the effectiveness of foundation model fusion. **b,** The ELF ensemble learning strategy significantly outperformed alternative aggregation methods using the same five tile-level foundation models ($P < 0.001$). Statistical significance was assessed using a two-sided Wilcoxon signed-rank test. All results are presented as means with standard deviation obtained from 1,000 bootstrap replicates.



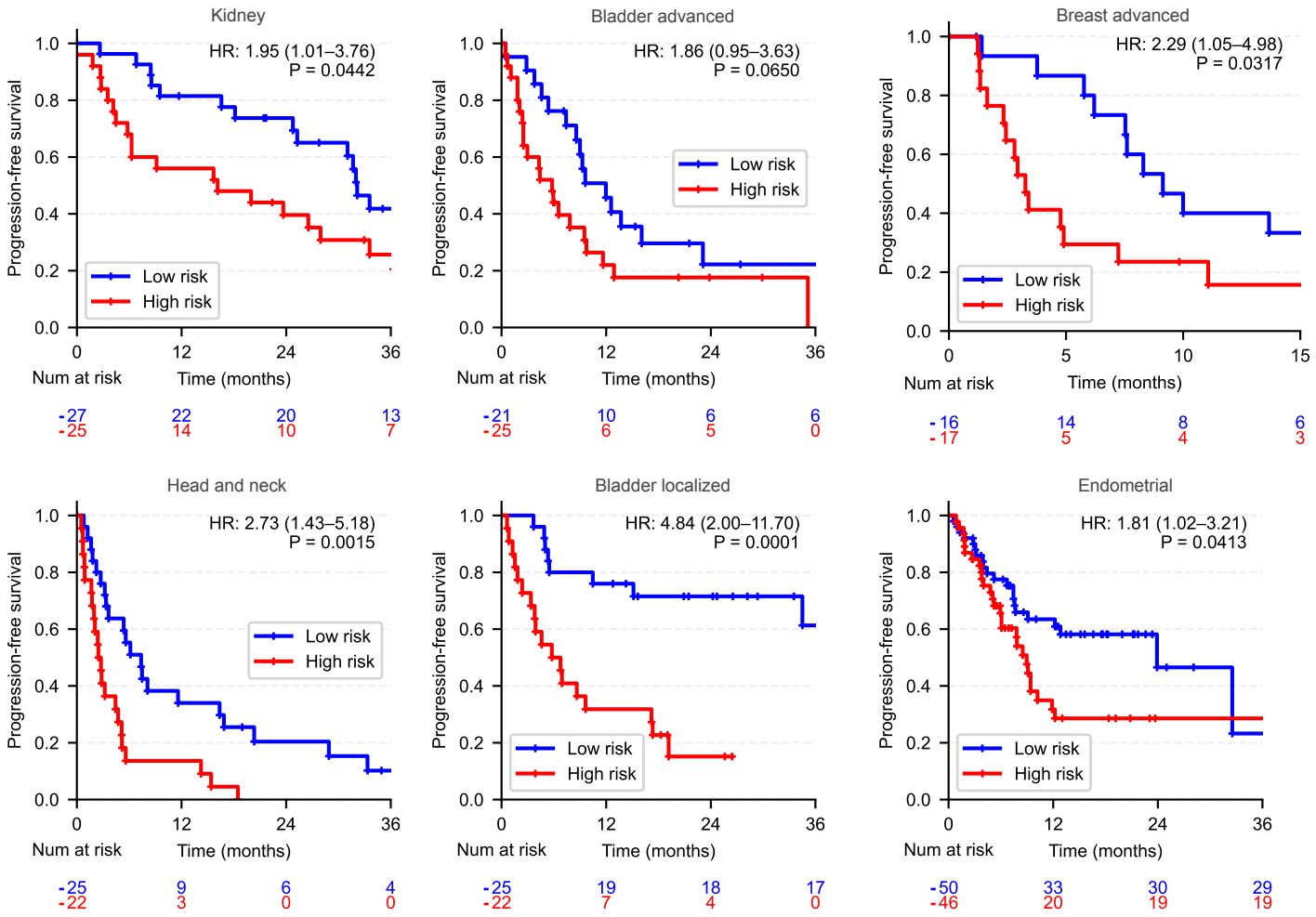
Extended Data Figure 6: **Detailed performance comparison of tumor mutational burden status prediction in the TCGA pan-cancer cohort between ELF and others.** ELF surpasses all baselines in both metrics of AUC and PPV (NPV > 0.95). The error bars represent the mean and standard error based on five-fold cross-validation results.



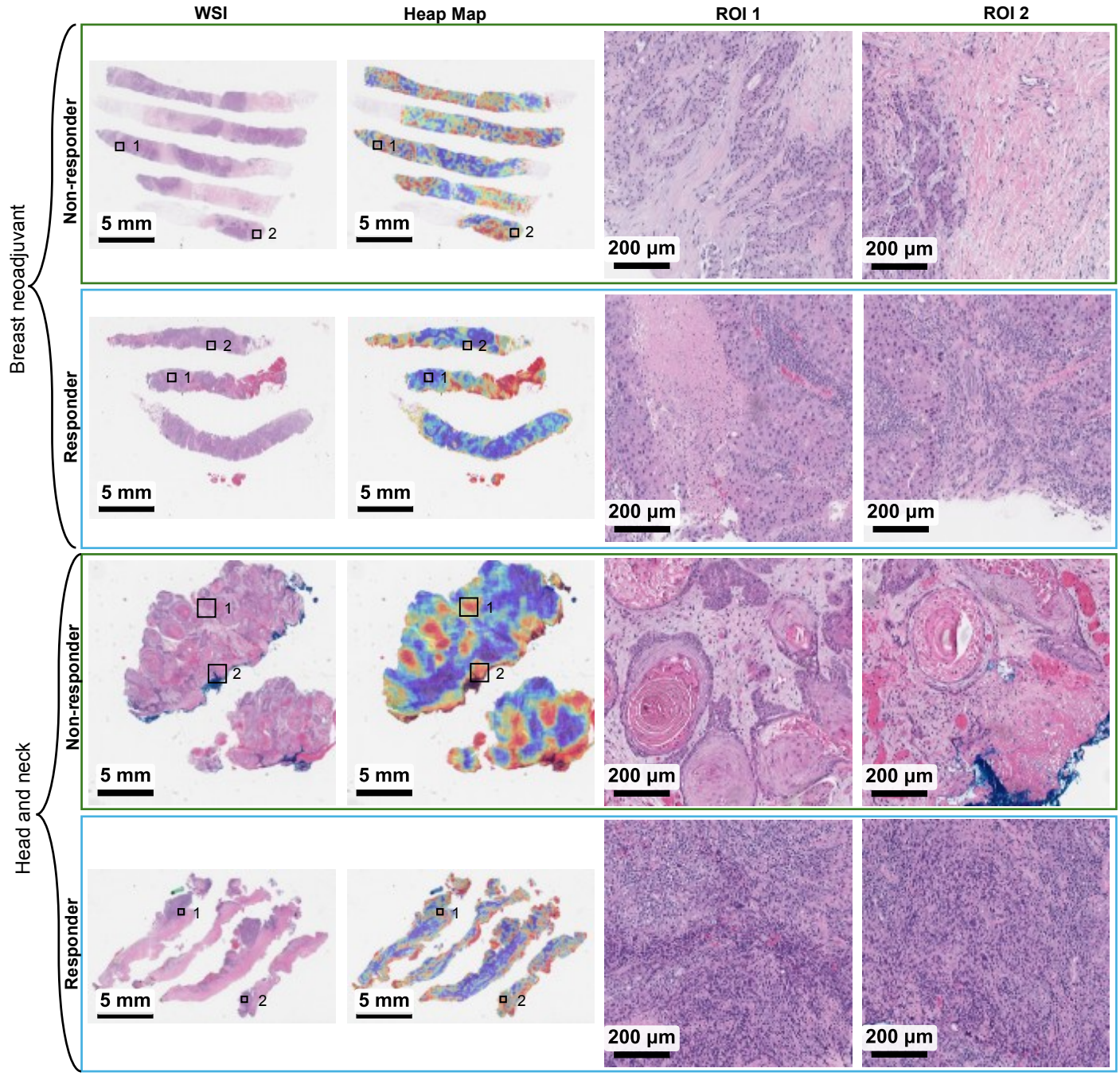
Extended Data Figure 7: **The performance of integrations of diverse foundation models and the ensemble strategy on the Breast (Chemotherapy) and Breast (Trastuzumab) cohorts. a,** ELF significantly outperformed individual foundation models for anticancer therapy response in two external cohorts ($P < 0.001$), confirming the effectiveness of foundation model fusion. **b,** The ELF ensemble learning strategy significantly outperformed alternative aggregation methods using the same five tile-level foundation models across two external cohorts ($P < 0.001$). Statistical significance was assessed using a two-sided Wilcoxon signed-rank test. All results are presented as means with standard deviation obtained from 1,000 bootstrap replicates.



Extended Data Figure 8: **The performance of integrations of diverse foundation models and the ensemble strategy on the Lung (CMB) and Breast advanced immunotherapy cohorts. a,** ELF significantly outperformed individual foundation models for anticancer therapy response in two external cohorts ($P < 0.001$), confirming the effectiveness of foundation model fusion. **b,** The ELF ensemble learning strategy significantly outperformed alternative aggregation methods using the same five tile-level foundation models across two external cohorts ($P < 0.001$). Statistical significance was assessed using a two-sided Wilcoxon signed-rank test. All results are presented as means with standard deviation obtained from 1,000 bootstrap replicates.



Extended Data Figure 9: **Kaplan-Meier analysis of PFS across immunotherapy cohorts**. Kaplan–Meier curves of PFS (stratified by the median ELF-predicted risk score) in the rest five cohorts showed that the ELF can stratify patients into high-risk and low-risk groups significantly, except the Bladder advanced cohort. Survival differences between high- and low-risk groups were assessed by a two-sided log-rank test.



Extended Data Figure 10: **Visualization comparison between the responder and non-responder.** All WSIs, heatmaps, and two regions of interest (ROI) with high attention score were represented from left to right. The first and second rows displayed two cases with and without response to immunotherapy from the Breast neoadjuvant cohort. The patient with response displays high intratumoral and peritumoral lymphoid infiltrates; high histologic grade with nuclear pleomorphism (ROI 1) and tumor necrosis with abundant inflammatory infiltrate (ROI 2). In contrast, the non-response patient shows a residual tumor has low histologic grade and dense intratumoral fibrosis with no tumor-infiltrating lymphocytes (ROI 1) and dense stromal fibrosis in the peritumoral region with minimal peritumoral inflammation (ROI 2). The last two rows displayed two head and neck cancer patients with and without response to immunotherapy. The patient with response shows the presence of tumor cells with marked pleomorphism and bizarre nuclei, and also with brisk tumor-infiltrating lymphocytes (ROI 1 and 2). On the other hand, the patient without response displays abundant intratumoral stroma containing dense collagen fibers with sparse lymphocytic infiltration (ROI 1) and marked fibrosis with dense collagen in the peritumoral stroma with sparse lymphocytic infiltration (ROI 2).

Extended Data Table 1: **Data distribution used for ELF pre-training.** The model development dataset consists of 53,699 WSIs across 20 main organs from multiple public datasets, such as GTEx, PANDA, etc.

Organ	Cancer (train/val)	No-Cancer (train/val)	Total
Adrenal	204/22	639/71	936
Bladder	433/48	117/12	610
Brain	486/53	2003/222	2764
Breast	1895/210	790/87	2982
Cervix	258/28	72/8	366
Colorectal	4038/448	3023/335	7844
Esophagus	142/16	2412/267	2837
Heart	0/0	3442/382	3824
Kidney	470/52	539/59	1120
Liver	502/55	543/60	1160
Lung	129/14	987/109	1239
Ovary	0/0	227/25	252
Pancreas	148/16	771/85	1020
Prostate	3001/333	7087/787	11208
Skin	2406/267	6246/691	9610
Spleen	0/0	780/86	866
Stomach	660/74	837/92	1663
Testis	229/25	528/58	840
Thyroid	468/53	804/89	1414
Uterus	536/59	495/54	1144
Total	16005/1773	32342/3579	53699

Extended Data Table 2: **Data distribution of disease subtyping datasets.**

Datasource	Organ	# Patients	# WSIs	# Classes	Train:Validation: Test
BCCC	Skin	-	1831	2	1434:0:397
BCCC	Skin	-	1831	3	1434:0:397
BCCC	Skin	-	1831	5	1434:0:397
BRACS	Breast	189	547	7	395:65:87
EBRAINS	Brain	2147	2319	12	1151:595:573
EBRAINS	Brain	2147	2319	30	1151:595:573

Extended Data Table 3: **Data distribution of biomarker predictions in the TCGA dataset.** All results are summarised at the patient level.

Biomarker	Cancer Type	Total patients	Positive patients	Negative patients
AKT1	CRC	500	11	489
ATM	BLCA	384	53	331
ATM	ESCA	155	6	149
ATM	LIHC	350	13	337
ATM	UCEC	473	92	381
BARD1	CRC	502	9	493
BRAF	CRC	500	59	441
BRAF	LGGGBM	721	18	703
BRAF	LUADLUSC	921	51	870
BRAF	SKCM	403	219	184
BRAF	THCA	486	286	200
BRCA1	CRC	502	14	488
BRCA1	UCEC	473	44	429
BRCA2	BRCA	1012	42	970
BRCA2	CRC	500	38	462
BRCA2	ESCA	155	6	149
BRCA2	UCEC	473	75	398
CCND1	BLCA	382	42	340
CCND1	BRCA	1030	158	872
CCND1	ESCA	155	52	103
CCND1	LUADLUSC	921	70	851
CCND1	PRAD	396	5	391
CCND1	SKCM	335	22	313
CCND1	UCEC	479	36	443
CDK4	LUADLUSC	921	30	891
CDK4	SKCM	246	43	203
CHEK2	UCEC	473	34	439
EGFR	LUADLUSC	918	106	812
ERBB2	BLCA	381	64	317
ERBB2	BRCA	1012	144	868
ERBB2	ESCA	155	25	130
ERBB2	LUADLUSC	918	34	884
ESR1	BRCA	1025	9	1016
ESR1	UCEC	473	40	433
FGFR2	BLCA	381	12	369
FGFR3	BLCA	381	65	316
FGFR3	LGGGBM	727	6	721
IDH1	LGGGBM	721	387	334
KIT	LGGGBM	857	51	806
KIT	SKCM	246	10	236
KRAS	BLCA	381	25	356
KRAS	BRCA	1025	6	1019

next page

Extended Data Table 3: **Data distribution of biomarker predictions in the TCGA dataset.** All results are summarised at the patient level.

Biomarker	Cancer Type	Total patients	Positive patients	Negative patients
KRAS	CRC	500	208	292
KRAS	ESCA	155	13	142
KRAS	LGGGBM	721	18	703
KRAS	LIHC	350	7	343
KRAS	LUADLUSC	921	151	770
KRAS	OV	92	16	76
KRAS	PAAD	177	115	62
KRAS	UCEC	479	95	384
MET	LUADLUSC	918	42	876
MLH1	CRC	502	20	482
NBN	CRC	500	9	491
NRAS	THCA	488	39	449
PIK3CA	BRCA	1012	358	654
PIK3CA	CRC	502	136	366
PIK3CA	LUADLUSC	918	239	679
PIK3CA	OV	92	20	72
PIK3CA	SKCM	246	7	239
POLE	UCEC	479	76	403
PTEN	CRC	500	43	457
PTEN	LUADLUSC	918	106	812
PTEN	PRAD	398	14	384
PTEN	UCEC	479	315	164
ROS1	LUADLUSC	921	6	915
TP53	BLCA	384	188	196
TP53	BRCA	1025	341	684
TP53	LIHC	350	112	238
TP53	LUADLUSC	918	625	293
TP53	SKCM	248	81	167
TSC1	LUADLUSC	921	16	905
TSC2	CRC	500	15	485
TSC2	LUADLUSC	921	27	894
TSC2	UCEC	479	37	442

Extended Data Table 4: **Data distribution of biomarker predictions across CRC cohorts.** All results are summarised at the patient level.

Dataset	Biomarker	Total patients	Positive patients	Negative patients	Evaluation
SR386	BRAF	400	45	355	Cross-validation
SR386	KRAS	400	137	263	Cross-validation
SR386	MSI	400	31	369	Cross-validation
SR1482	BRAF	338	61	277	External-validation
SR1482	KRAS	399	177	222	External-validation
SR1482	MSI	129	16	113	External-validation
MCO	BRAF	1488	173	1315	External-validation
MCO	KRAS	1490	455	1035	External-validation
MCO	MSI	1488	195	1293	External-validation
TCGA-CRC	BRAF	501	58	443	External-validation
TCGA-CRC	KRAS	501	207	294	External-validation
TCGA-CRC	MSI	429	61	368	External-validation

Extended Data Table 5: **Data distribution of the aneuploidy scores regression task at the TCGA dataset.** All results are summarised at the patient level.

Cancer Type	# Patients	# WSIs	Score range	Train: Validation: Test
Pan-cancer	8819	10854	0-39	6163:889:1767

Extended Data Table 6: **Data distribution of the Whole Genome Doubling (WGD) and Tumor Mutational Burden (TMB) classification tasks at the TCGA pan-cancer dataset.** All results are summarised at the patient level.

Biomarker	# Patients	# WSIs	Positive patients	Negative patients	Train: Validation: Test
WGD	8819	10854	3094	5725	6163:889:1767
TMB	8200	10102	701	7781	6560:0:1640

Extended Data Table 7: **Data distribution of anticancer therapy cohorts.** All results are summarised at the patient level.

Dataset	Treatment	Total patients	Responder	Non-Responser	Evaluation
Metastatic breast (Platinum)	Chemotherapy	77	33	44	Cross-validation
Breast (Trastuzmab, Yale)	Trastuzumab	85	36	49	Cross-validation
Ovarian (Platinum)	Chemotherapy	158	91	67	Cross-validation
Ovarian (Bevacizumab)	Bevacizumab	36	25	11	Cross-validation
Bladder (BCG)	BCG	131	43	88	Cross-validation
Breast (Chemotherapy, TransNEO)	Chemotherapy	116	26	90	Cross-validation
Breast (Chemotherapy, IMPRESS)	Chemotherapy	64	27	37	External-validation
Breast (Trastuzumab, TransNEO)	Trastuzumab	81	31	50	Cross-validation
Breast (Trastuzumab, IMPRESS)	Trastuzumab	62	38	24	External-validation

Extended Data Table 8: **Data distribution of anti-PD1/PD-L1 immunotherapy cohorts.** All results are summarised at the patient level.

Dataset	Total patients	Durable Responder	Non-Durable Responser	Evaluation
Bladder advanced	46	27	19	Cross-validation
Bladder localized	47	14	33	Cross-validation
Kidney	52	43	9	Cross-validation
Non-metastatic melanoma	63	31	32	Cross-validation
Metastatic melanoma	78	58	20	Cross-validation
Head and neck	47	16	31	Cross-validation
Gastroesophageal	106	50	56	Cross-validation
Endometrial	96	59	37	Cross-validation
Lung (Stanford)	148	81	67	Cross-validation
Lung (CMB)	34	18	16	External-validation
Breast neoadjuvant	32	15	17	Cross-validation
Breast advanced	33	17	16	External-validation

Extended Data Table 9: **Detailed performance of biomarker prediction across internal and external CRC cohorts.** PPV: Positive Predictive Value; NPV: Negative Predictive Value. All results are summarised at the patient level.

Dataset	Biomarker	Method	Evaluation	AUC	Accuracy	Sensitivity	Specificity	PPV	NPV
SR386	BRAF	ELF	Cross-validation	**0.843**	**0.805**	0.756	0.811	**0.414**	0.963
SR386	BRAF	TITAN	Cross-validation	0.765	0.678	0.778	0.665	0.385	0.960
SR386	BRAF	CHIEF	Cross-validation	0.795	0.708	0.756	0.701	0.259	0.963
SR386	BRAF	Prov-GigaPath	Cross-validation	0.804	0.740	0.511	0.769	0.241	0.936
SR386	KRAS	ELF	Cross-validation	**0.729**	0.558	0.860	0.399	**0.436**	0.904
SR386	KRAS	TITAN	Cross-validation	0.661	0.520	0.882	0.330	0.424	0.916
SR386	KRAS	CHIEF	Cross-validation	0.697	0.497	0.870	0.305	0.421	0.918
SR386	KRAS	Prov-GigaPath	Cross-validation	0.658	**0.612**	0.694	0.570	0.462	0.792
SR386	MSI	ELF	Cross-validation	**0.923**	0.917	0.648	0.940	0.511	0.969
SR386	MSI	TITAN	Cross-validation	0.911	0.840	0.614	0.859	**0.533**	0.967
SR386	MSI	CHIEF	Cross-validation	0.844	0.780	0.800	0.777	0.288	0.983
SR386	MSI	Prov-GigaPath	Cross-validation	0.892	**0.920**	0.548	0.951	0.513	0.962
SR1482	BRAF	ELF	External-validation	**0.776**	0.524	0.918	0.437	0.264	0.960
SR1482	BRAF	TITAN	External-validation	0.765	**0.609**	0.869	0.552	**0.299**	0.950
SR1482	BRAF	CHIEF	External-validation	0.688	0.405	0.951	0.285	0.227	0.963
SR1482	BRAF	Prov-GigaPath	External-validation	0.711	0.293	1.000	0.137	0.203	1.000
SR1482	KRAS	ELF	External-validation	**0.649**	0.474	1.000	0.054	**0.457**	1.000
SR1482	KRAS	TITAN	External-validation	0.528	0.449	1.000	0.009	0.446	1.000
SR1482	KRAS	CHIEF	External-validation	0.586	0.451	1.000	0.014	0.447	1.000
SR1482	KRAS	Prov-GigaPath	External-validation	0.619	**0.584**	0.542	0.617	0.530	0.628
SR1482	MSI	ELF	External-validation	**0.871**	**0.845**	0.688	0.867	**0.423**	0.951
SR1482	MSI	TITAN	External-validation	0.688	0.791	0.562	0.823	0.310	0.930
SR1482	MSI	CHIEF	External-validation	0.811	0.682	0.875	0.655	0.264	0.974
SR1482	MSI	Prov-GigaPath	External-validation	0.798	0.667	0.875	0.637	0.255	0.973
MCO	BRAF	ELF	External-validation	**0.843**	**0.813**	0.688	0.830	**0.347**	0.953
MCO	BRAF	TITAN	External-validation	0.769	0.749	0.705	0.755	0.275	0.951
MCO	BRAF	CHIEF	External-validation	0.800	0.706	0.792	0.694	0.254	0.962
MCO	BRAF	Prov-GigaPath	External-validation	0.625	**0.880**	0.006	0.995	0.143	0.884
MCO	KRAS	ELF	External-validation	**0.636**	0.328	0.998	0.034	**0.312**	0.972
MCO	KRAS	TITAN	External-validation	0.558	0.308	1.000	0.004	0.306	1.000
MCO	KRAS	CHIEF	External-validation	0.592	0.306	1.000	0.001	0.306	1.000
MCO	KRAS	Prov-GigaPath	External-validation	0.557	**0.587**	0.396	0.671	0.345	0.716
MCO	MSI	ELF	External-validation	**0.897**	**0.886**	0.682	0.916	**0.552**	0.950
MCO	MSI	TITAN	External-validation	0.742	0.517	0.846	0.468	0.193	0.953
MCO	MSI	CHIEF	External-validation	0.878	0.852	0.738	0.869	0.460	0.957
MCO	MSI	Prov-GigaPath	External-validation	0.795	0.691	0.764	0.680	0.265	0.950
TCGA-CRC	BRAF	ELF	External-validation	**0.762**	**0.677**	0.741	0.668	**0.226**	0.952
TCGA-CRC	BRAF	TITAN	External-validation	0.684	0.397	0.914	0.330	0.151	0.967
TCGA-CRC	BRAF	CHIEF	External-validation	0.754	0.547	0.810	0.512	0.179	0.954
TCGA-CRC	BRAF	Prov-GigaPath	External-validation	0.632	0.453	0.845	0.402	0.156	0.952
TCGA-CRC	KRAS	ELF	External-validation	**0.622**	0.415	1.000	0.003	0.414	1.000
TCGA-CRC	KRAS	TITAN	External-validation	0.564	0.417	1.000	0.007	**0.415**	1.000
TCGA-CRC	KRAS	CHIEF	External-validation	0.585	**0.419**	0.986	0.020	0.415	0.667
TCGA-CRC	KRAS	Prov-GigaPath	External-validation	0.592	0.415	1.000	0.003	0.414	1.000
TCGA-CRC	MSI	ELF	External-validation	**0.857**	**0.841**	0.738	0.859	**0.464**	0.952
TCGA-CRC	MSI	TITAN	External-validation	0.698	0.438	0.902	0.361	0.190	0.957
TCGA-CRC	MSI	CHIEF	External-validation	0.854	0.830	0.738	0.845	0.441	0.951
TCGA-CRC	MSI	Prov-GigaPath	External-validation	0.815	0.774	0.787	0.772	0.364	0.956

References

1. Bera, K., Schalper, K. A., Rimm, D. L., Velcheti, V. & Madabhushi, A. Artificial intelligence in digital pathology—new tools for diagnosis and precision oncology. *Nature reviews Clinical oncology* **16**, 703–715 (2019).

2. Yates, J. & Van Allen, E. M. New horizons at the interface of artificial intelligence and translational cancer research. *Cancer Cell* **43**, 708–727 (2025).

3. Bhinder, B., Gilvary, C., Madhukar, N. S. & Elemento, O. Artificial intelligence in cancer research and precision medicine. *Cancer discovery* **11**, 900–915 (2021).

4. Van der Laak, J., Litjens, G. & Ciompi, F. Deep learning in histopathology: the path to the clinic. *Nature medicine* **27**, 775–784 (2021).

5. Xu, H. *et al.* A whole-slide foundation model for digital pathology from real-world data. *Nature* **630**, 181–188 (2024).

6. Wang, X. *et al.* A pathology foundation model for cancer diagnosis and prognosis prediction. *Nature* **634**, 970–978 (2024).

7. Xiang, J. *et al.* A vision–language foundation model for precision oncology. *Nature* 1–10 (2025).

8. Saillard, C. *et al.* H-optimus-0 (2024). URL `https://github.com/bioptimus/releases/tree/main/models/h-optimus/v0`.

9. Chen, R. J. *et al.* Towards a general-purpose foundation model for computational pathology. *Nature Medicine* **30**, 850–862 (2024).

10. Lu, M. Y. *et al.* A visual-language foundation model for computational pathology. *Nature Medicine* **30**, 863–874 (2024).

11. Vorontsov, E. *et al.* A foundation model for clinical-grade computational pathology and rare cancers detection. *Nature medicine* **30**, 2924–2935 (2024).

12. Wang, X. *et al.* Foundation model for predicting prognosis and adjuvant therapy benefit from digital pathology in gi cancers. *Journal of Clinical Oncology* JCO–24 (2025).

13. Campanella, G. *et al.* Real-world deployment of a fine-tuned pathology foundation model for lung cancer biomarker detection. *Nature Medicine* 1–9 (2025).

14. Kondepudi, A. *et al.* Foundation models for fast, label-free detection of glioma infiltration. *Nature* **637**, 439–445 (2025).

15. Lipkova, J. & Kather, J. N. The age of foundation models. *Nature Reviews Clinical Oncology* **21**, 769–770 (2024).

16. Chen, X., Xie, S. & He, K. An empirical study of training self-supervised vision transformers. In *Proceedings of the IEEE/CVF international conference on computer vision*, 9640–9649 (2021).

17. He, K. *et al.* Masked autoencoders are scalable vision learners. In *Proceedings of the IEEE/CVF conference on computer vision and pattern recognition*, 16000–16009 (2022).

18. Neidlinger, P. *et al.* Benchmarking foundation models as feature extractors for weakly-supervised computational pathology. *arXiv preprint arXiv:2408.15823* (2024).

19. Ma, J. *et al.* Towards a generalizable pathology foundation model via unified knowledge distillation. *arXiv preprint arXiv:2407.18449* (2024).

20. Ma, J. *et al.* Pathbench: A comprehensive comparison benchmark for pathology foundation models towards precision oncology. *arXiv preprint arXiv:2505.20202* (2025).

21. Campanella, G. *et al.* A clinical benchmark of public self-supervised pathology foundation models. *Nature Communications* **16**, 3640 (2025).

22. Ding, T. *et al.* Multimodal whole slide foundation model for pathology. *arXiv preprint arXiv:2411.19666* (2024).

23. Zimmermann, E. *et al.* Virchow2: Scaling self-supervised mixed magnification models in pathology. *arXiv preprint arXiv:2408.00738* (2024).

24. Yacob, F. *et al.* Weakly supervised detection and classification of basal cell carcinoma using graph-transformer on whole slide images. *Scientific Reports* **13**, 7555 (2023).

25. Brancati, N. *et al.* Bracs: A dataset for breast carcinoma subtyping in h&e histology images. *Database* **2022**, baac093 (2022).

26. Roetzer-Pejrimovsky, T. *et al.* The digital brain tumour atlas, an open histopathology resource. *Scientific Data* **9**, 55 (2022).

27. Taylor, A. M. *et al.* Genomic and functional approaches to understanding cancer aneuploidy. *Cancer cell* **33**, 676–689 (2018).

28. Prelaj, A. *et al.* Artificial intelligence for predictive biomarker discovery in immuno-oncology: a systematic review. *Annals of Oncology* **35**, 29–65 (2024).

29. Weinstein, J. N. *et al.* The cancer genome atlas pan-cancer analysis project. *Nature genetics* **45**, 1113–1120 (2013).

30. Myles, C., Um, I. H., Marshall, C., Harris-Birtill, D. & Harrison, D. J. Surgen: 1020 h&e-stained whole slide images with survival and genetic markers. *arXiv preprint arXiv:2502.04946* (2025).

31. Ward, R. Mco study whole slide image collection (2015).

32. Jonnagaddala, J. *et al.* Integration and analysis of heterogeneous colorectal cancer data for translational research. In *Nursing Informatics 2016*, 387–391 (IOS Press, 2016).

33. Quinton, R. J. *et al.* Whole-genome doubling confers unique genetic vulnerabilities on tumour cells. *Nature* **590**, 492–497 (2021).

34. Lambuta, R. A. *et al.* Whole-genome doubling drives oncogenic loss of chromatin segregation. *Nature* **615**, 925–933 (2023).

35. Yarchoan, M., Hopkins, A. & Jaffee, E. M. Tumor mutational burden and response rate to pd-1 inhibition. *New England Journal of Medicine* **377**, 2500–2501 (2017).

36. Marcus, L. *et al.* Fda approval summary: pembrolizumab for the treatment of tumor mutational burden–high solid tumors. *Clinical Cancer Research* **27**, 4685–4689 (2021).

37. Passaro, A. *et al.* Cancer biomarkers: Emerging trends and clinical implications for personalized treatment. *Cell* **187**, 1617–1635 (2024).

38. Hoang, D.-T. *et al.* A deep-learning framework to predict cancer treatment response from histopathology images through imputed transcriptomics. *Nature cancer* **5**, 1305–1317 (2024).

39. Bergstrom, E. N. *et al.* Deep learning artificial intelligence predicts homologous recombination deficiency and platinum response from histologic slides. *Journal of Clinical Oncology* **42**, 3550–3560 (2024).

40. Chowdhury, S. *et al.* Proteogenomic analysis of chemo-refractory high-grade serous ovarian cancer. *Cell* **186**, 3476–3498 (2023).

41. Farahmand, S. *et al.* Her2 and trastuzumab treatment response h&e slides with tumor roi annotations. *The Cancer Imaging Archive)* (2022).

42. Wang, C.-W. *et al.* Histopathological whole slide image dataset for classification of treatment effectiveness to ovarian cancer. *Scientific Data* **9**, 25 (2022).

43. Schouten, D. *et al.* Combining histology, medical imaging and molecular data for medical prognosis and diagnosis (chimera) (2025). URL `https://doi.org/10.5281/zenodo.15045553`.

44. Sammut, S.-J. *et al.* Multi-omic machine learning predictor of breast cancer therapy response. *Nature* **601**, 623–629 (2022).

45. Huang, Z. *et al.* Artificial intelligence reveals features associated with breast cancer neoadjuvant chemotherapy responses from multi-stain histopathologic images. *NPJ precision oncology* **7**, 14 (2023).

46. Cristescu, R. *et al.* Pan-tumor genomic biomarkers for pd-1 checkpoint blockade–based immunotherapy. *Science* **362**, eaar3593 (2018).

47. Samstein, R. M. *et al.* Tumor mutational load predicts survival after immunotherapy across multiple cancer types. *Nature genetics* **51**, 202–206 (2019).

48. Nabet, B. Y. *et al.* Noninvasive early identification of therapeutic benefit from immune checkpoint inhibition. *Cell* **183**, 363–376 (2020).

49. Louie, B. H. *et al.* Molecular tumor board for unicorns: Outcomes for rare and ultra-rare cancers using an n-of-one personalized treatment strategy. *Iscience* **27** (2024).

50. Conrads, T. P. & Petricoin III, E. F. The obama administration's cancer moonshot: a call for proteomics. *Clinical Cancer Research* **22**, 4556–4558 (2016).

51. Bagaev, A. *et al.* Conserved pan-cancer microenvironment subtypes predict response to immunotherapy. *Cancer cell* **39**, 845–865 (2021).

52. Wang, X. *et al.* Transformer-based unsupervised contrastive learning for histopathological image classification. *Medical image analysis* **81**, 102559 (2022).

53. Lenz, T. *et al.* Unsupervised foundation model-agnostic slide-level representation learning. In *Proceedings of the Computer Vision and Pattern Recognition Conference*, 30807–30817 (2025).

54. Vanguri, R. S. *et al.* Multimodal integration of radiology, pathology and genomics for prediction of response to pd-(l) 1 blockade in patients with non-small cell lung cancer. *Nature cancer* **3**, 1151–1164 (2022).

55. Weitz, P. *et al.* The acrobat 2022 challenge: automatic registration of breast cancer tissue. *Medical image analysis* **97**, 103257 (2024).

56. Xu, F. *et al.* Predicting axillary lymph node metastasis in early breast cancer using deep learning on primary tumor biopsy slides. *Frontiers in oncology* **11**, 759007 (2021).

57. Geijs, D. J. *et al.* Detection and subtyping of basal cell carcinoma in whole-slide histopathology using weakly-supervised learning. *Medical Image Analysis* **93**, 103063 (2024).

58. Zhu, M. *et al.* Development and evaluation of a deep neural network for histologic classification of renal cell carcinoma on biopsy and surgical resection slides. *Scientific reports* **11**, 7080 (2021).

59. Wei, J. W. *et al.* Pathologist-level classification of histologic patterns on resected lung adenocarcinoma slides with deep neural networks. *Scientific reports* **9**, 3358 (2019).

60. Lonsdale, J. *et al.* The genotype-tissue expression (gtex) project. *Nature genetics* **45**, 580–585 (2013).

61. Neto, P. C. *et al.* imil4path: A semi-supervised interpretable approach for colorectal whole-slide images. *Cancers* **14**, 2489 (2022).

62. Neto, P. C. *et al.* An interpretable machine learning system for colorectal cancer diagnosis from pathology slides. *NPJ precision oncology* **8**, 56 (2024).

63. Chauhan, E. *et al.* Ipd-brain: An indian histopathology dataset for glioma subtype classification. *Scientific Data* **11**, 1403 (2024).

64. Zhang, Z. *et al.* Pathologist-level interpretable whole-slide cancer diagnosis with deep learning. *Nature Machine Intelligence* **1**, 236–245 (2019).

65. Kim, Y. J. *et al.* Paip 2019: Liver cancer segmentation challenge. *Medical image analysis* **67**, 101854 (2021).

66. Bulten, W. *et al.* Artificial intelligence for diagnosis and gleason grading of prostate cancer: the panda challenge. *Nature medicine* **28**, 154–163 (2022).

67. Ilse, M., Tomczak, J. & Welling, M. Attention-based deep multiple instance learning. In *International conference on machine learning*, 2127–2136 (PMLR, 2018).

68. Lu, M. Y. *et al.* Data-efficient and weakly supervised computational pathology on whole-slide images. *Nature biomedical engineering* **5**, 555–570 (2021).

69. El Nahhas, O. S. *et al.* From whole-slide image to biomarker prediction: end-to-end weakly supervised deep learning in computational pathology. *Nature Protocols* **20**, 293–316 (2025).

70. Vaidya, A. *et al.* Molecular-driven foundation model for oncologic pathology. *arXiv preprint arXiv:2501.16652* (2025).

71. Oord, A. v. d., Li, Y. & Vinyals, O. Representation learning with contrastive predictive coding. *arXiv preprint arXiv:1807.03748* (2018).

72. Chen, T. & Guestrin, C. Xgboost: A scalable tree boosting system. In *Proceedings of the 22nd acm sigkdd international conference on knowledge discovery and data mining*, 785–794 (2016).

73. Wang, Y. K. *et al.* Screen them all: high-throughput pan-cancer genetic and phenotypic biomarker screening from h&e whole slide images. *arXiv preprint arXiv:2408.09554* (2024).

74. Swanton, C. My cancer genome: a unified genomics and clinical trial portal. *The Lancet Oncology* **13**, 668–669 (2012).

75. Suehnholz, S. *et al.* Oncokb, a precision oncology knowledgebase. *Cancer Research* **80**, 3208–3208 (2020).

76. Callahan, A. *et al.* The stanford medicine data science ecosystem for clinical and translational research. *JAMIA open* **6**, ooad054 (2023).